
Article:
Nevin, C., Geddes, D.A., Thorpe, C.L. et al. (2026) Mass transport behaviour of caesium and strontium in geopolymer cements. Journal of Materials Chemistry A. ISSN: 2050-7488

https://doi.org/10.1039/d5ta08377j

Journal of Materials Chemistry A

ROYAL SOCIETY OF CHEMISTRY

PAPER

View Article Online
View Journal

Cite this: DOI: 10.1039/d5ta08377j

Mass transport behaviour of caesium and strontium in geopolymer cements

Charlotte Nevin,[a] Daniel A. Geddes,[a] Clare L. Thorpe,[a] Martin C. Stennett,[a] Tom J. Wilkinson,[a] Latham T. Haigh,[a] Dinu Iuga[b] and Brant Walkley *[a]

Geopolymers are a promising alternative to conventional Portland cement-based wasteforms for immobilising hazardous radioactive fission products such as caesium-137 and strontium-90, offering superior durability and lower leach rates. However, the specific mass transport mechanisms governing radionuclide release in geopolymers remain poorly understood, limiting implementation. This study reveals the incorporation and mass transport mechanisms of caesium (Cs) and strontium (Sr) in metakaolin-based geopolymers. Solid-state characterisation showed Sr incorporation *via* direct chemical binding in the alkali aluminosilicate hydrate gel in charge-balancing extra-framework sites, replacing K^+ ions, and precipitation of $SrCO_3$ and $Sr(OH)_2$, while Cs is predominantly bound within the charge-balancing sites in the alkali aluminosilicate gel. Leach testing confirmed low overall release rates, with all measured leachability indices significantly exceeding the industry minimum of 6 (Li >13 for Cs; Li >18 for Sr), outperforming conventional PC systems. Mass transport modelling revealed distinct mechanisms: Cs release is accurately described by a Diffusion/Surface Exchange Kinetics Model (DSEM), yielding high correlation (R^2 > 0.99), however, Sr exhibited a complex, staggered release profile. Standard mass transport models (diffusion, dissolution, surface exchange) could not satisfactorily capture this complex behaviour. We hypothesise this rate resumption is caused by the structural reordering or crystallisation of the amorphous K–A–S–H gel into a zeolitic phase, potentially excluding incorporated Sr. This finding highlights that simple diffusive models, commonly assumed for geopolymers, are inadequate for predicting the long-term performance of Sr-containing geopolymer wasteforms. The new insight presented here is critical development of geopolymers for radioactive waste disposal.

Received 14th October 2025
Accepted 1st December 2025

DOI: 10.1039/d5ta08377j

rsc.li/materials-a

1 Introduction

Radioactive waste, generated from nuclear power and other applications, for example medical isotope production (such as cobalt-60 or technicium-99), poses significant environmental and societal hazards. Safe conditioning and disposal of this waste is therefore essential, particularly for legacy sites requiring remediation.[1] Caesium-137 (Cs-137) and strontium-90 (Sr-90) are two particularly abundant radionuclides produced in the fission reaction of uranium-235 (U-235), and are prevalent in wastes streams from civil nuclear operations and from major nuclear accidents. For example, they are found together in waste streams such as complex sludges and slurries at the Sellafield nuclear site in the UK and contaminated groundwater at Fukushima Daichi Nuclear Power Plant in Japan. Their medium-term half-life (~30 years), high radiotoxicity, water solubility, and biological mimicry[2] make them particularly harmful to human health and the environment, and necessitate robust wasteforms to immobilise them for hundreds of years.

Currently, in the UK, intermediate level waste (ILW) and low level waste (LLW), including those containing Cs-137 and Sr-90, are encapsulated in specifically formulated Portland cement (PC)/blast furnace slag (BFS) blends. These cement formulations have traditionally been used due to their simplicity, high throughput, low cost, and secure availability. However, PC/BFS systems exhibit limitations including high leaching rates and variable Cs retention depending on their C–S–A ratios.[3,4] Furthermore, BFS supply chain vulnerabilities in the UK, due to the closure of blast furnaces in the steel sector, highlight the need for alternative disposal technologies.[5]

Geopolymer cements have been highlighted as a potential alternative material for the cementation of radioactive waste due to their superior physiochemical properties, their cation binding sites providing capability to immobilise certain cations (*e.g.* Cs^+ and Sr^{2+}), their lower leach rates, and their improved durability in extreme conditions, including high temperatures and acidic environments.[5] Geopolymers comprise a structurally disordered, highly cross-linked alkali aluminosilicate gel (denoted (N,K)–A–S–H, as Na^+ and K^+ are the most common cations) that exhibits a pseudo-zeolitic structure, with the alkali cations in extra-framework sites balancing the negative charge

[a]School of Chemical, Materials, and Biological Engineering, University of Sheffield, UK. E-mail: b.walkley@sheffield.ac.uk
[b]Department of Physics, University of Warwick, Coventry, UK

arising from Al^{3+} ion tetrahedral coordination.[6] If energetically favourable, the alkali cations may be substituted with other alkali or alkaline earth cations *via* ion exchange processes. This provides the ability to chemically bind and immobilise Cs^{+} and Sr^{2+} in the alkali aluminosilicate gel, in addition to physical encapsulation of the waste.[1,7] The International Atomic Energy Agency (IAEA) standard leach tests assume diffusion as the dominating mass transport mechanisms governing the movement of Cs and Sr in geopolymers and other cements.[8] However, the mass transport mechanisms in geopolymers have not been widely studied, especially regarding applications in radioactive waste disposal.

There have been numerous studies assessing leaching of different species from geopolymers (such as cadmium, copper, lead, zinc, chromium, cobalt, strontium, caesium, and other cations) under various conditions, but the mechanisms governing this leaching are rarely explored. Similar studies have been performed for Portland cement and blast furnace slag cements, such as early work done by Côtê[9] and more recent studies by Abdel-Rahman[10,11] and El-Kamash,[12] which found that releases were governed by complex, multi-parametric mass transport. El-Kamash also studied mass transport in zeolites and Portland cement.[13] These studies defined mass transport processes (diffusion, dissolution, and surface exchange/reaction) from first principles and fit these to experimental release data, collected from leaching experiments. Generally, it was found that diffusion and surface reactions dominated release in these studies.[10] However, similar investigations for geopolymers are lacking.

This work aims to address this knowledge gap by investigating the mass transport mechanisms of Cs and Sr in metakaolin-based geopolymer cements using stable isotopes to represent Sr-90 and Cs-137. It quantifies and elucidates the release mechanisms, contributing to the development of safer and more durable radioactive waste disposal technologies.

2 Experimental methods

2.1 Sample preparation

Geopolymer cements were produced by reaction of a solid metakaolin powder (MetaMax, Lawrence Industries, with composition determined by X-ray fluorescence as shown in Table 1) and a potassium silicate solution (PQ-silicates, solution modulus $SiO_2/K_2O = 1.0$). Stoichiometry was designed to obtain a nominal chemical composition of $K_2O/Al_2O_3 = 1$, $SiO_2/Al_2O_3 = 3$, $H_2O/K_2O = 13$.[1,14] Samples containing non-radioactive isotopes of Cs and Sr were prepared by mixing 1 or 3 wt% $Sr(OH)_2$ or CsOH as a solid powder with the metakaolin prior to addition of the activating solution. Samples were subsequently mixed for 10 minutes at 1200 rpm using a high shear mixer to achieve homogeneity, cast in sealed cylindrical containers, and cured at 20 ± 2 °C for 28 days.

After curing, samples were removed from sealed containers and formed into cylinders (13 mm length, 14 mm diameter) with the ends sealed with araldite to prevent axial mass transfer. Samples underwent a leach test according to a modified ASTM C1308 standard, wherein the monolithic samples were fully submerged in deionised water which was sampled and fully replaced at 2 hours, 7 hours, 24 hours, every day until 11 days, and then at 14 days, 21 days, 28 days, and 35 days. After the last time point, the monoliths were removed from solution and submerged in isopropanol to remove any bound water through ion exchange to prevent further reaction. The samples were then prepared for characterisation of the solid phase by hand grinding with a pestle and mortar until a talc-like consistency was reached. Samples for SEM or EPMA were left as solid monoliths and prepared as described in Section 2.2.

Table 1 Metakaolin chemical composition (wt%) as determined by X-ray fluorescence. LOI = loss on ignition at 1000 °C

SiO_2	Al_2O_3	K_2O	Na_2O	MgO	TiO_2	Fe_2O_3	Other	LOI
52.5	44.5	0.2	0.2	< 0.05	1.3	0.4	0.2	0.6

2.2 Characterisation of the solid phase

2.2.1 X-ray diffraction (XRD). A Panalytical X'Pert^3 Powder X-ray Diffractometer with Cu Kα radiation, a nickel filter, a step size of 0.020°, and a count time of 1 s per step was used to obtain XRD data across a 2θ range of 5–70°. To reduce diffracted background intensity at low angles, an anti-scatter blade was used with an incident beam divergence of 1.0 mm. Within the diffracted beam, a 2.5° Soller slit was used. Peak analysis and identification was performed using Diffrac.EVA software and the ICCD database.

2.2.2 Scanning electron microscopy with energy dispersive X-ray spectroscopy (SEM-EDX). Samples to be analysed by SEM were prepared by sealing in epoxy resin and subsequently grinding and polishing the surface using an Automet 250. Isopropanol was used as the grinding solution which does not interact with the cement matrix.[15] Grit paper P600 was used to expose the samples, followed by P800, P1200, P2500, and P4000 until a smooth surface was achieved. 3 μm, 1 μm, and 0.25 μm oil-based diamond suspensions were used to obtain a mirror finish by polishing on a polishing pad. The samples were carbon coated to a thickness of between 30 and 40 nm and a strip of electrically conducting silver paint was added before analysis to reduce charge buildup on the sample during analysis. A Hitachi TM3030 instrument with 20 kV accelerating voltage, a working distance of 8 mm, and a backscatter detector was used to obtain SEM images. To allow for elemental identification and qualitative compositional information, high-energy Energy Dispersive X-ray (EDX) analysis was used. Scans were taken for 600 s; after this point no further increase in the signal/noise of the EDX spectra was observed.

2.2.3 Electron probe microscopy analysis (EPMA). To obtain more detailed compositional information, EPMA was performed using a Joel 8350F PLUS HYPERBROBE equipped with Energy Dispersive X-ray and Wavelength Dispersive X-ray (4 channel) systems. The samples were analysed using 10 kV and 10 nA beam conditions with a peak coating time of 40 s and two background measurements (upper and lower) for 20 s. The analytical setup was as follows; Al and Si measured on channel 1 with TAP crystal, Cs and Sr measured on channel 2 with PETL

crystal, Ti and K measured on channel 3 with PETH crystal, and Na measured on channel 4 with TAPH crystal. Elemental maps were obtained at 80×, 120×, 1000×, and 1500× magnification.

2.2.4 Fourier transform infrared (FTIR) spectroscopy. Attenuated total reflectance (ATR)-FTIR spectra for powdered samples were measured across a range of 400 to 4000 cm^{-1} using a Thermo Fischer Nicolet iS 5 Spectrometer scanning 64 times at a resolution of 16 cm^{-1} and a zinc selenide crystal. A background spectrum was always measured before the first sample and automatically removed from the spectrum for each sample. Plots are generated with transmission normalised between [0,1] to allow comparison between spectra.

2.2.5 Nuclear magnetic resonance (NMR) spectroscopy. Solid state single pulse ^{29}Si and ^{27}Al magic angle spinning (MAS) and cross polarisation (CP) ^{1}H–^{29}Si MAS NMR data were obtained for each sample to examine the local structure around atomic nuclei. Spectra were acquired on a Bruker Avance III HD 500 spectrometer at 11.7 T (B_0) using a 4.0 mm dual resonance CP/MAS probe with a Larmor frequency of 99.35 MHz for ^{29}Si and 130.32 MHz for ^{27}Al. ^{27}Al MAS spectra were acquired using a 1.7 μs non-selective ($\pi/2$) excitation pulse, a measured 10 s relaxation delay, spinning at 12.5 kHz, and a total of 128 scans. ^{29}Si MAS spectra were acquired using a 5.5 μs non-selective ($\pi/2$) excitation pulse, a measured 90 s relaxation delay, spinning at 12.5 kHz with a total of 256 scans. CP MAS spectra were acquired with a ^{29}Si 1.7 μs non-selective ($\pi/2$) pulse width, an initial ^{1}H 2.5 μs non-selective ($\pi/2$) pulse width, a recycle delay of 1.5 s, a Hartmann–Hahn contact period of 1.7 ms, a spinning frequency of 12.5 kHz, and a total of 10 240 scans collected. Additionally, a nominal ^{1}H decoupling field strength of 80 kHz was employed during acquisition.[1]

^{133}Cs SS MAS NMR experiments were performed at the National High Field NMR facility at The University of Warwick, UK, to probe the local environment of the Cs nuclei. Spectra were acquired on a Bruker Avance NEO HFXY spectrometer with a MAS III spinning speed controller, using the 4 mm HX (low gamma) H13892 probe. ^{133}Cs spectra were acquired at 20.0 T (B_0) with a Larmour frequency of 111.5 MHz, using a rotor synchronised double frequency sweep echo pulse, a measured 0.1 s relaxation delay, spinning at 20.0 MHz, and a total of 86 000 scans.

High-field solid state ^{39}K MAS NMR data were acquired at 20.0 T ($\nu_0 = 39.67$ MHz) using a Bruker Avance Neo 850 spectrometer with a Bruker 4.0 mm HX MAS probe, which enabled a spinning rate of 14 kHz to be implemented. Pulse calibration and chemical shift referencing for all ^{39}K data were achieved using KCl(s) ($\delta_{iso} = 47.8$ ppm) as a secondary reference to the IUPAC primary reference of 0.1 M KCl(aq) ($\delta_{iso} = 0$ ppm). A 'non-selective' $\pi/2$ pulse of 12 μs was measured allowing for a 'selective' 4 μs $\pi/3$ to be implemented. Spectra were acquired using a Hahn echo pulse sequence ($\pi/2$–τ–π–acquire) using a measured relaxation delay of 0.1 s and acquiring a total of 480 000 transients per spectra.

2.2.6 X-ray absorption spectroscopy (XAS). XAS was used to measure the Sr and potassium K-edge features (16 keV and 3.6 keV, respectively) and the Cs L-edge features (5 keV) on the bending magnet beamline B18 at Diamond Light Source (DLS) Synchrotron in Harwell, Oxfordshire, UK. Measurements were conducted on the core XAS B18 beamline which covers 2.05–35 keV energy range. The design of B18 has three main optical elements: a collimating mirror, a water-cooled double crystal monochromator, and a focusing mirror. For this study, an unfocused beam was used with a Cr/Pt mirror coating, and a Si(111) monochromator. Pellets were produced using finely ground cement powders, combined with polyethylene glycol to give samples with a thickness equal to 2 absorption lengths. Incident and transmitted beam intensities were measured using ionisation chambers, filled with mixtures of He and Ar or N^2, operated in a stable region of their I/V curve. Yttrium foil was measured to provide an absolute energy calibration; the first inflection point (in the first derivative) was defined to be 17 133 eV. The yttrium foil was measured periodically to ensure that there was no energy drift over the course of the experiment. Data reduction and analysis was performed using the Demeter software package, specifically Athena and Artemis.

Cs K-edge (35.98 keV) XAS spectra were collected on the XMaS beamline at the European Synchrotron Radiation Facility (ESRF) in transmission, covering the 35.7–36.9 keV energy range.

2.3 Characterisation of the aqueous phase

2.3.1 Inductively coupled plasma-mass spectroscopy (ICP-MS). Aqueous samples were analysed for Cs and Sr concentrations using ICP-MS (Thermo Fisher iCAP RQ with an ESI Prep-Fast 4DX autosampler). Concentrations were determined by suitable dilution into 2% (v/v) nitric acid as per standard operating procedures. Calibration curves were prepared by measuring intensities against a series of known calibration standards, which were prepared by diluting single element standard solutions (Fisher Scientific) with 2% (v/v) nitric acid. The ICP data were used to calculate the Cumulative Fraction Leached (CFL) as described in eqn (1).

$$\mathrm{CFL} = \frac{\sum a_n}{A_0} \quad (1)$$

where a_n is the concentration of radionuclide measured and A_0 is the initial concentration at $t = 0$.

3 Mass transport models

In order to determine the mass transfer mechanisms leading to leaching of the Cs and Sr from geopolymers, models must be developed describing the main mass transport processes, including diffusion, dissolution, surface exchange kinetics, and combinations thereof. The mass transfer models are outlined subsequently, as developed from previous literature.[9–11] Using the curve fit tool from the SciPy package in Python, an optimised fit is achieved between the experimental data from the leach tests and the models outlined subsequently. Statistical analysis is performed to understand the goodness of fit of each model and therefore to determine the best-fitting descriptive model of the CFL behaviour.

3.1 Diffusive mass transport

It is commonly assumed that, after the initial period of surface wash-off, the leaching behaviour of certain radionuclides is controlled by diffusion.[16] To model this, an assumption of diffusion through a semi-infinite cylinder (no axial diffusion due to the ends of the cylindrical monolit being sealed), and therefore the solution of Fick's law in a semi-infinite medium can be applied (eqn (2)) as follows:

$$J(t) = \frac{\partial C}{\partial t} = D_e \frac{\partial^2 C}{\partial r^2} \quad (2)$$

where C is the concentration of contaminant (mg m^{-3}), t is the time, D_e is the effective diffusion coefficient (m^2 s^{-1}), and r is the one-dimensional coordinate/radius (m). For diffusive behaviour, the cumulative fraction leached (CFL) is the flux ($J(t)$), and therefore the solution can be written as follows (eqn (3)):

$$\mathrm{CFL} = \frac{\sum a_n}{A_0} = 2\frac{S}{V}\sqrt{\frac{Dt}{\pi}} \quad (3)$$

where S is the surface area (cm^2) and V is the volume (cm^3) of the sample.

3.2 Dissolutive mass transport

As the Cs and Sr can form a structurally significant part of the geopolymer due to the potential ion exchange with potassium, the release into solution of these radionuclides can cause a structural change to the matrix. Dissolution behaviour is shown in eqn (4), which assumes a release controlled by the dissolution constant.

$$\mathrm{CFL} = \frac{\sum a_n}{A_0} = \left(\frac{S}{V}\right) Ut \quad (4)$$

where U_0 is the dissolution constant.

3.3 Surface exchange kinetics

Surface phenomena contribute to the mass transport of species from a cementitious or glass wasteform, described based on the kinetics of exchanges between the surface of a solid and the aqueous solution. The descriptive model for this is shown in eqn (5).

$$\mathrm{CFL} = \frac{\sum a_n}{A_0} = C(1 - \exp[kt]) \quad (5)$$

where C and k are constants based on the initial wash off rate and the exchanges between the surface of the wasteform and the aqueous solution.

3.4 Combined mass transport

3.4.1 Diffusion/dissolution model (DDM). In this model, the mass transfer is assumed to take place due to diffusion through the pores of the geopolymer and through dissolution of the waste matrix, simultaneously. The model is shown in eqn (6).

$$\mathrm{CFL} = \frac{\sum a_n}{A_0} = \left(\frac{S}{V}\right) \times \left(2\sqrt{\frac{Dt}{\pi}} + U_0 t\right) \quad (6)$$

3.4.2 Diffusion/surface exchange kinetics model (DSEM). In this model, the mass transfer is assumed to take place due to diffusion through the pores and through exchange kinetics between the leachate and the waste matrix on the outer edge. The model is shown in eqn (7).

$$\mathrm{CLF} = \frac{\sum a_n}{A_0} = 2\frac{S}{V}\left(\sqrt{\frac{Dt}{\pi}}\right) + k_1(1 - \exp[kt]) \quad (7)$$

3.4.3 Dissolution/surface exchange kinetics model. In this model, the mass transfer is assumed to occur solely due to dissolution of the waste matrix and exchange between the leachate and the waste matrix. The model is shown in eqn (8).

$$\mathrm{CLF} = \frac{\sum a_n}{A_0} = k_1(1 - \exp[kt]) + \left(\frac{S}{V}\right) U_0 t \quad (8)$$

3.5 Leachability index (L_i)

In stabilisation/solidification (S/S) of radioactive and other hazardous wastes, the leachability index ($L_{(i)}$) is an indicative parameter for determining the effectiveness of a waste matrix. L_i is the logarithm of the effective diffusivity of the radionuclide of interest and a waste form is considered to have acceptable leachability if L_i is greater than 6. The leachability index can be calculated with eqn (9).

$$L_i = \log\left[\frac{\beta}{D_e}\right] \quad (9)$$

where $\beta = 1.0$ cm^2 s^{-1} is a defined constant.

3.6 Statistical analysis

3.6.1 R^2 value. The R^2 value, or the coefficient of determination, is a statistical measure which provides information about the goodness of fit of a model. R^2 is calculated by eqn (10), *i.e.* the sum of the residuals squared divided by the sum of the distance the data is away from the mean all squared, taken from 1. An R^2 of 1 indicates a perfect fit of the model to the data and 0 (or less) indicates no correlation between the model and the data.

$$R^2 = 1 - \frac{\text{sum squared regression(SSR)}}{\text{total sum of squares(SST)}} \quad (10)$$

4 Results and discussion

4.1 Cumulative fraction leached

Geopolymer cements loaded with 1 and 3 wt% $Sr(OH)_2$ or CsOH were prepared and leached as described, in deionised water held at 20 °C in a temperature-controlled environment chamber. At the discrete leaching time points, aliquots of the leachate were extracted and analysed by ICP-MS analysis to quantify the release of Cs and Sr from the waste matrix. The cumulative fraction leached (CFL) for both cations, shown in

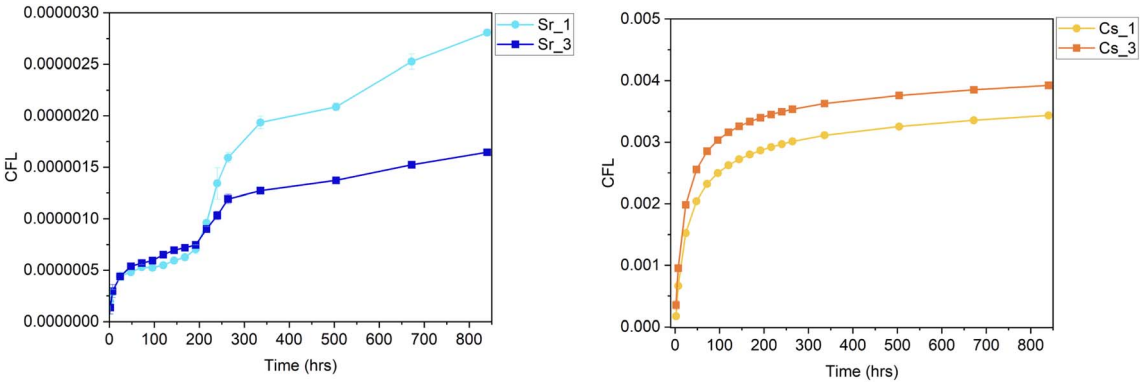

Fig. 1 Sr (left) and Cs (right) cumulative fraction leached (CFL) with varying incorporation of Cs and Sr into the geopolymer matrix. Sr or Cs refers to the radionuclide of interest and 1 or 3 refers to the mass% of its addition in hydroxide form.

Fig. 1, represents the ratio of the released radionuclide concentration to its initial mass within the geopolymer matrix. All measurements were performed in triplicate, and the reported data represent the mean of these replicates. The error bars are small, especially for Cs, indicating high reproducibility and consistency due to adherence to standardised methodology.

The pH rose to 11.00 during the first 24 hours, remained above 11 for the 48 hours time point and thereafter dropped a little remaining pH 10 $\pm$ 0.5 until the end of the 35 days experiment. In the bulk solution the maximum Cs and Sr concentrations measured were 30 ppm and 0.006 ppm respectively. Solution modelling in PHREEQC-2 confirmed that the bulk solution was undersaturated with regard to Sr and Cs bearing phases throughout the experiment (although this does not rule out supersaturation within the matrix pores or localised to the material surface). The solution was, however, intermittently supersaturated with regard to aluminium hydroxide and aluminium-silicate phases (see SI, Tables 3 and 4) and became increasingly supersaturated as the pH dropped below 10.5.

Overall, the Cs release profile exhibits a smooth increase, characterised by rapid initial release (<200 hours), followed by a plateau. Conversely, the Sr release profile exhibits a more complex staggered release pattern, with a period of release then stabilisation, followed by a subsequent rate resumption period at ~200 hours and further stabilisation.

The observed CFL profiles reveal a larger release for Cs (total 30 000 and 100 000 ppb of Cs for the 1 and 3% CsOH samples, respectively) compared to Sr (total 23.5 and 36.1 ppb for the 1 and 3% $Sr(OH)_2$ samples, respectively). This difference likely arises due to the differences in the solubility and incorporation of the cations. Sr may remain present as undissolved $Sr(OH)_2$, partition to $SrCO_3$, or occupy partially Sr-substituted zeolite sites.[1,14,17] $SrCO_3$ is highly stable and practically insoluble in water; therefore Sr release may be dependent on the precipitation and dissolution of this phase.

Cs tends to occupy the zeolitic domain within the K–A–S–H gel[17–19] but previous work has shown that there is selectivity for K^+ over Cs^+ into these sites.[20] Therefore, when K occupies available exchangeable sites, Cs is excluded from these hosts and its retention becomes governed by diffusion or surface exchange, making it more readily leachable. The solid-state characterisation in this work has provided some evidence that Sr is present as discrete Sr-rich phases whilst Cs is evenly distributed through the K–A–S–H matrix and therefore it is likely this that is causing an increase in the leachability of Cs compared with Sr. There is evidence of $SrCO_3$ forming in the higher loaded samples analysed by XAS analysis.

Notably, the Sr release (as a percentage of Sr added) from the lower loading samples (1%) is larger than that of the higher loading sample (3%) after ~200 hours. In both systems the total amount of strontium released over the experiment is similar (approximately 30% higher in the higher 3% Sr system *vs.* the 1% Sr system instead of the 300% that might be expected). This observation is unexpected, as a higher loading would typically be expected to result in a higher CFL. However, it is possible that a Sr saturation limit is reached for $SrCO_3$, meaning that a relatively higher proportion of the added Sr is bound in this poorly soluble mineral phase and a lower proportion incorporated into less soluble phases or sorbed to mineral surfaces that would be more easily released from the sample.

The staggered release behaviour of Sr mirrors trends observed in glass systems where crystallisation of secondary phases on the surface of the glass consumes silica from the protective amorphous gel layer and surrounding solution leading to a resumption of dissolution of the glass matrix.[21–23] This phenomenon is usually observed in aluminosilicate glass compositions subjected to high pH and high temperatures that promote precipitation of zeolites.[23,24] Given the structural similarities between the K–A–S–H gel and aluminosilicate glasses, it is possible that the leaching mechanisms may be somewhat analogous. Although solution replacement throughout the ASTM C1308 leach test is intended to simulate semi-dynamic leaching, the bulk solution was intermittently supersaturated with regard to Al and Si and, furthermore, the test is not agitated meaning that supersaturation and secondary phase formation likely occurred in pores and where localised concentration gradients occurred at the sample surface. It is also possible that crystallisation of the initially amorphous gel layer could cause a release of Sr that was previously incorporated into the K–A–S–H gel but that substitutes to a lesser extent into the newly formed mineral or zeolite phases.

Table 2 Calculated diffusion coefficients and associated leachability indices for Sr and Cs

Sample	D_e ($cm^2\ s^{-1}$)	L_i
Sr_1	$2.2 \times 10^{-19} \pm 3.4 \times 10^{-23}$	18.7 ± 0.00007
Sr_3	$7.8 \times 10^{-20} \pm 1.9 \times 10^{-24}$	19.1 ± 0.00001
Cs_1	$5.4 \times 10^{-14} \pm 1.6 \times 10^{-18}$	13.3 ± 0.00001
Cs_3	$6.0 \times 10^{-14} \pm 3.1 \times 10^{-18}$	13.2 ± 0.00002

This presents implications for waste disposal, as deviations from expected phases or from expected diffusive leaching behaviour could affect predictive modelling. Deviations from the long-term modelling may result in an uncontrolled, underestimated radionuclide release after repository closure.

Using the CFL, the effective diffusivity coefficient can be calculated from the slope of the straight line (m) of the plot of CFL *versus* $t^{\frac{1}{2}}$ using eqn (11).

$$D_e = \pi\left(\frac{mV}{2S}\right)^2 \quad (11)$$

where V is the volume of the sample (cm^3) and S is the effective surface area of the sample (cm^2).

Using the relation above, the effective diffusion coefficient and associated L_i (calculated from eqn (9)) were calculated and are displayed in Table 2.

All L_i values significantly exceed the industry minimum expected value of 6, even accounting for error on the calculation of D_e. Additionally, conventional PC systems typically exhibit $L_i \approx 10$ for Sr and $L_i \approx 7.5$ for Cs.[25] Therefore, geopolymers show superior performance under these conditions when compared with PC.

4.2 Effect of leaching on the solid phase

4.2.1 X-ray diffraction. The XRD diffractograms shown in the SI, Fig. 2 are consistent with the formation of an aluminosilicate gel. The broad peak centred at 29° 2θ is attributed to diffuse scattering from the amorphous K–A–S–H gel, as expected for geopolymers.[1] Sharper, less intense peaks at 25°, 38°, 38.5°, 48°, 50°, 54°, 55°, and 62°correspond to crystalline reflections consistent with anatase and quartz, respectively, originating as small impurities in the precursor or sand used in sample preparation. At 52° 2θ on the Cs_3_Post sample there is a small, crystalline peak. This could be attributed to a different impurity, including quartz or trace iron[26] or due to the formation of a potential Cs-aluminosilicate phase under these

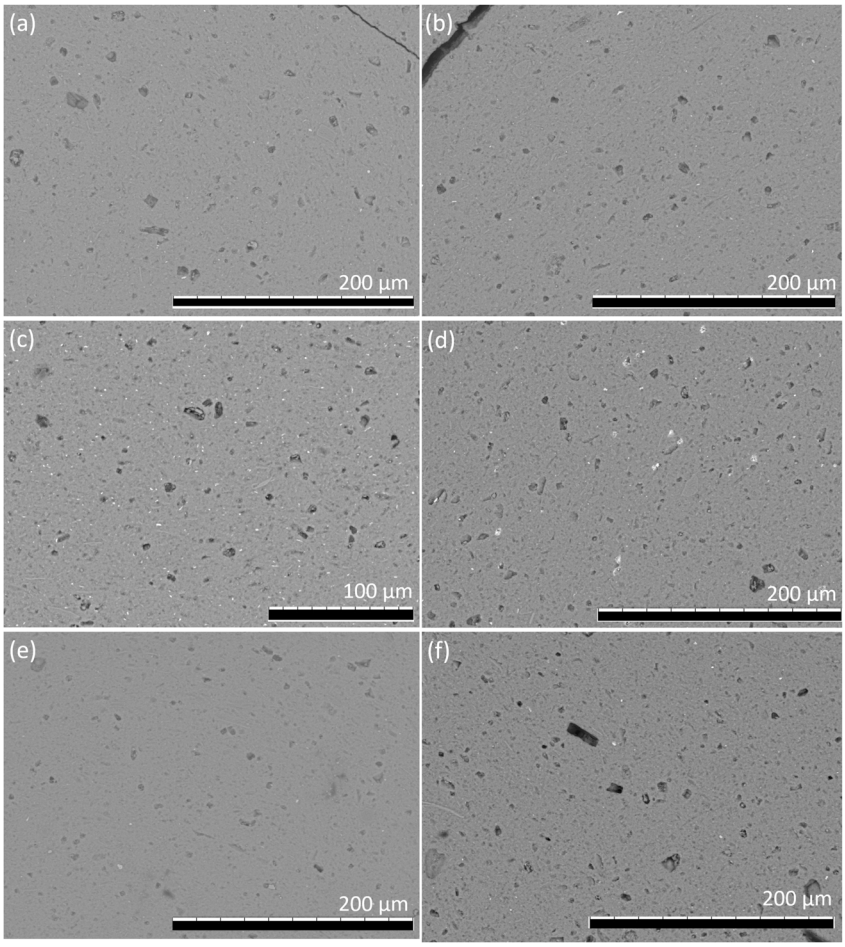

Fig. 2 SEM images of the bulk structure for (a) C_0_Pre, (b) C_0_Post, (c) Sr_3_Pre, (d) Sr_3_Post, (e) Cs_3_Pre, and (f) Cs_3_Post. Cs and Sr refer to the radionuclide of interest, with 1 and 3 refering to its mass% addition. C refers to 'control', with no Cs or Sr added.

conditions.[27] Due to the tendency of Cs to occupy the zeolitic domains in the K–A–S–H gel, it is likely the latter. No other crystalline phases were detected in the geopolymer gel.

Overall, the XRD diffractogram remains consistent after leaching. Therefore, it can be concluded that the leaching process did not significantly alter the bulk crystalline or amorphous phases within the geopolymers. However, as XRD was performed on a small volume of size reduced material, phases present as <1% of the total (*e.g.* surface precipitates) would not be detected by XRD.

4.2.2 Scanning electron microscopy with energy dispersive X-ray dispersive spectroscopy and electron probe microscopy analysis. To examine the bulk structure of the samples both before and after leaching and to assess the spatial composition of the samples, SEM-EDX was used to investigate select samples. These samples were selected to give a representative view of the microstructure before and after leaching and after incorporation of Sr and Cs.

The SEM images (Fig. 2) reveal a relatively homogeneous cross-sectional surface with a high number of pores, displaying no clear observable differences in the bulk sample before and after leaching or due to incorporation of Sr or Cs.

Low-resolution EDX mapping of the bulk of the samples (see SI, Fig. 3–5), indicated a homogeneous element distribution across all samples, with minimal elemental clustering. Post-leaching, an increased Si/Al ratio was observed indicated by the colouring of the maps, particularly in the 3% sample. This is consistent with the NMR findings (Section 4.2.4). Regions of high potassium content, likely due to residual potassium hydroxide or silicate in the pore solution, are present.

Due to oxygen interference with the elemental energy levels of Cs and Sr, EPMA was used for more accurate spatial distribution of elements and mass ratio quantification within the bulk geopolymer. The scans were taken of the samples loaded with 3% CsOH or $Sr(OH)_2$. EPMA scans reveal a relatively homogeneous cross-sectional surface with some element clustering. In the bulk sample, silicon, aluminium, and potassium are evenly distributed, except in the pore regions where measurements were unable to be ascertained. Areas of high aluminium content, corresponding to low potassium content, suggest the presence of unreacted metakaolin which is characterised by a lower Si/Al ratio than a geopolymer. High potassium regions corroborated the EDX findings, indicating residual potassium hydroxide or silicate in the pores.

Sr-containing samples showed Sr distribution in the matrix of approximately 1%, with localised areas up to 40% Sr. These areas were depleted in silicon, aluminium, and potassium, therefore they are likely either undissolved $Sr(OH)_2$ due to its low solubility

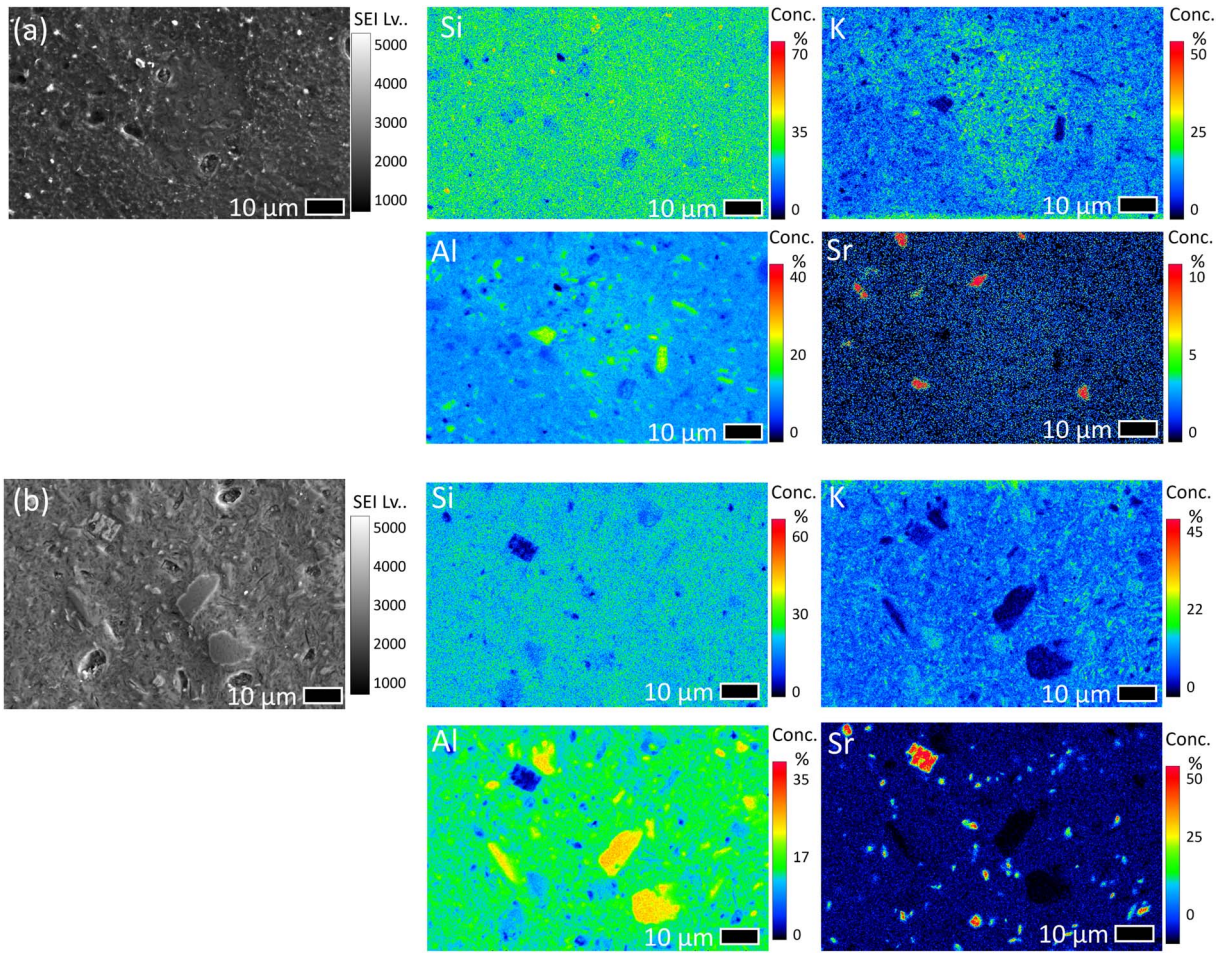

Fig. 3 EPMA scans for (a) Sr_3_Pre and (b) Sr_3_Post. Scans are for Al, Sr, Si, and K.

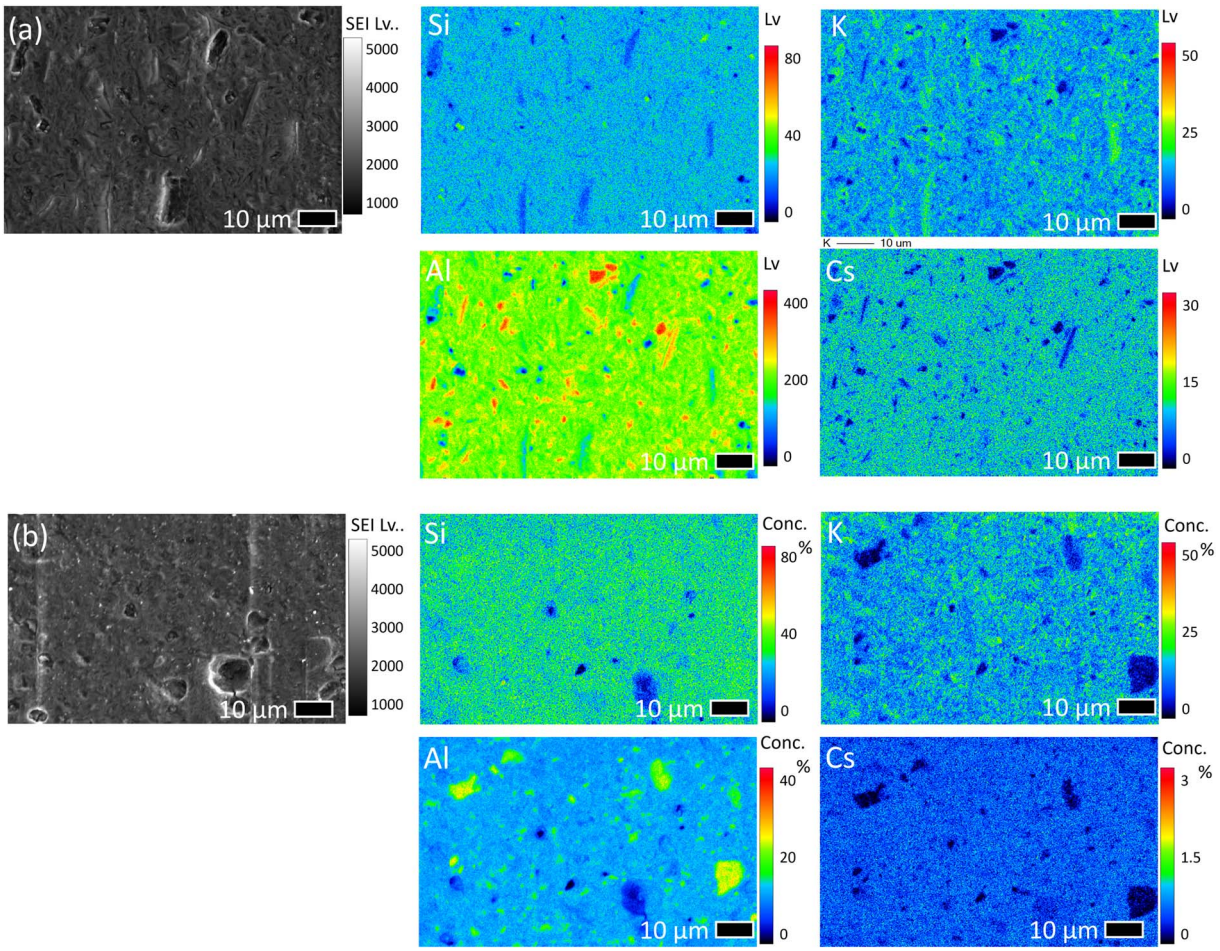

Fig. 4 EPMA scans for (a) Cs_3_Pre and (b) Cs_3_Post. Scans are for Al, Ca, Si, and K.

or the formation of $SrCO_3$ due to carbon present in the porewater. In contrast, Cs distribution was more uniform, likely due to the higher solubility of CsOH under the reaction mixture conditions. Overall, no significant visual differences were observed between the pre- and post-leach samples in the bulk phase.

Elemental quantification was performed on the bulk matrix and specific points of interest. Table 3 presents the average bulk matrix compositions and Table 4 details the point-of-interest compositions. The bulk matrix composition was determined by averaging elemental quantifications from discrete spots within the geopolymer, as shown in the image in Fig. 5.

In the bulk matrix, oxygen, silicon, aluminium, and potassium have the highest elemental concentrations, as expected for geopolymer gel. The Si/Al ratio is approximately 1.6, decreasing slightly after leaching (this is assessed more accurately in Section 4.2.4). Bulk Cs concentration is just below the expected 3% loading, decreasing significantly after leaching as a significant quantity is lost from the sample, as shown in Section 4.1. However, bulk Sr concentration is lower than expected, at 1% pre-leach, and are the same (within error) after leaching.

There EPMA scans reveal some heterogeneity, and there are some specific points of interest, for which elemental quantification was performed. These include 'bright spots', as shown in Fig. 5. The composition of these spots was determined and is shown in Table 4.

The high Sr concentration (up to 40%) of the bright particles (spot 1 on the pre-leach and both spots on the post-leach), alongside low silicon, aluminium, and potassium levels, indicate localised $Sr(OH)_2$ or $SrCO_3$ clusters (the presence of carbon could not be positively ascertained due to the carbon coating used on the samples). However, point 2 on the Sr pre-leach sample closely resembles the bulk composition, with a slightly elevated Sr concentration.

Conversely, for the Cs points of interest, the bright particles show minimal Cs and elevated titanium levels (up to 50%). Titanium, present in the metakaolin precursor, may form TiO_2 during dissolution, although its concentration varied considerably as indicated by the high standard deviation. Point 2 on the pre-leach sample, also shows elevated titanium levels, also with an increase in Cs levels. This could be because the Cs sorbed onto the titanium-rich clusters. Finally, the bright region on the post-leach sample (point 2) is largely similar to the bulk matrix.

Overall, the imaging reveals no significant changes to the bulk matrix as a result of leaching. However, it is likely that any significant changes due to dissolution would be visible in approximately the first 10 microns from the outside of the

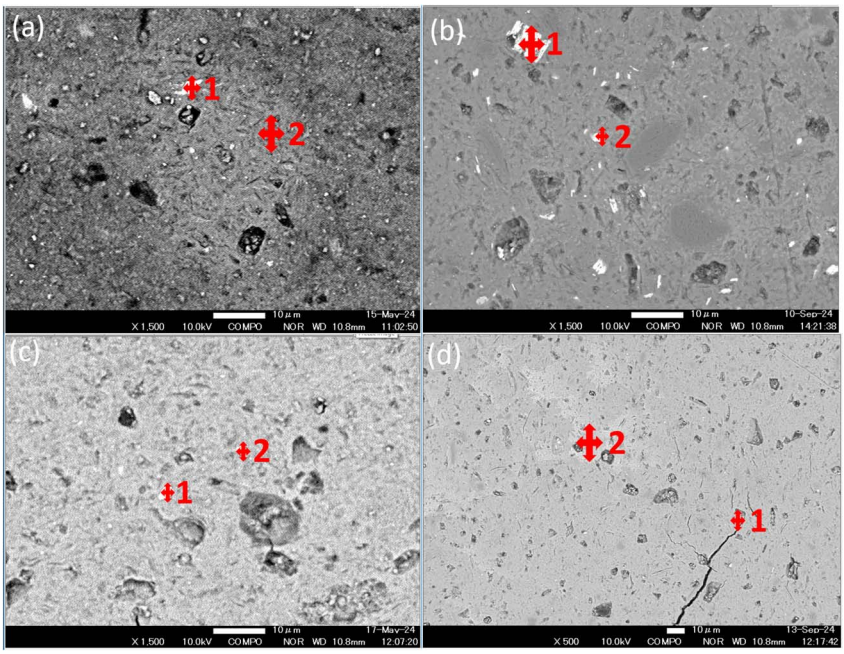

Fig. 5 Points of interest indicated by a cross. (a) Sr_3_Pre (1 = bright spot, 2 = bright region), (b) Sr_3_Post (1 = bright spot, 2 = bright spot), (c) Cs_3_Pre (1 = bright spot, 2 = bright spot), (d) Cs_3_Post (1 = bright spot, 2 = bright region).

Table 3 Composition of bulk matrix, as obtained from EPMA. Cs or Sr refers to the cation of interest for the sample

	Sr_3_Pre		Sr_3_Post		Cs_3_Pre		Cs_3_Post	
Species	Mean (%)	SD	Mean (%)	SD	Mean (%)	SD	Mean (%)	SD
Al	15.96	0.67	12.54	0.91	17.50	0.64	19.85	1.91
Si	25.52	0.81	19.57	0.90	21.79	1.07	25.90	2.28
K	10.00	1.11	14.55	2.60	13.00	2.49	7.83	2.66
O	46.03	0.51	51.39	1.12	43.76	0.97	43.20	2.82
Ti	0.21	0.12	0.41	0.46	0.57	0.59	1.89	4.63
Cs/Sr	0.97	0.18	1.49	0.49	2.84	0.45	0.90	0.40

sample. Low resolution scans are included in the SI and do not indicate any significant alteration at this magnitude, but more detailed scans could reveal insights into the potential formation of a leaching front or different phases.

4.2.3 Fourier transform infrared spectroscopy. The FTIR spectra for all pre- and post-leached samples (SI, Fig. 7) are all consistent with the formation of a geopolymer gel. The prominent, broad peak between 900–1200 cm^{-1} is indicative of the

Table 4 Composition of points of interest. Cs or Sr refers to the cation of interest for the sample. For more information as to what the points of interest are, see Fig. 5

		Sr_3_Pre		Sr_3_Post		Cs_3_Pre		Cs_3_Post	
Species	Point	Mean (%)	SD	Mean (%)	SD	Mean (%)	SD	Mean (%)	SD
Al	1	12.41	1.47	9.91	0.47	0.717	—	5.33	5.06
	2	16.16	1.38	4.11	0.72	9.54	—	20.26	0.58
Si	1	18.49	1.40	17.72	1.26	0.657	—	7.46	8.22
	2	23.06	0.74	7.73	1.87	13.78	—	26.14	2.42
K	1	7.64	3.19	6.035	2.67	0.993	—	2.45	2.39
	2	14.87		6.01	2.66	9.64	—	7.55	3.33
O	1	38.34	0.35	38.84	0.59	39.93	—	60.15	4.25
	2	44.11	1.32	35.42	0.64	41.61	—	44.27	6.57
Sr/Cs	1	21.98	1.70	25.80	1.37	0.0	—	0.18	1.38
	2	1.71	0.17	46.38	0.98	2.33	—	0.80	1.53

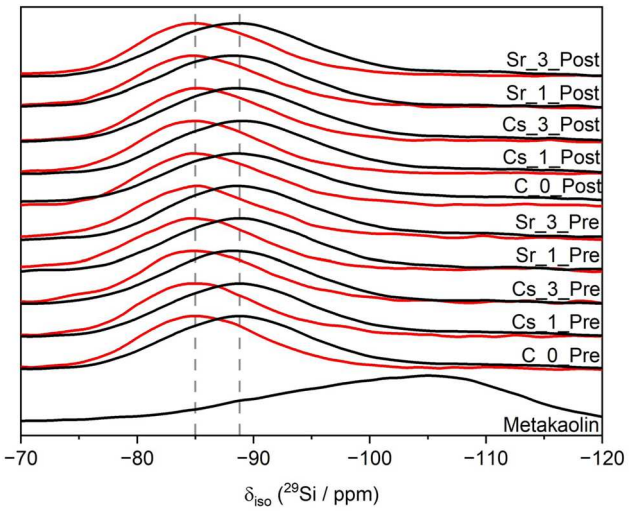

Fig. 6 ^{29}Si MAS ($B_0 = 11.7$ T, $\nu_R = 12.5$ kHz, shown in black) NMR and ^{1}H–^{29}Si CPMAS ($B^0 = 11.7$ T, $\nu_R = 12.5$ kHz and Hartmann–Hahn contact period $t = 1.7$ ms, shown in red) NMR spectra.

asymmetric stretching of T–O–T bonds (where T = Al or Si) within the aluminosilicate gel.[28] A subtle peak within the broad peak at 950 cm^{-1} is observed in the Cs_1_Post-leaching sample, suggesting the formation of a heterogeneously mixed alkali aluminosilicate gel, specifically an aluminium-rich region, as this tends to shift slightly towards a lower wavenumber. This formation is likely influenced by an increase in the Sr^{2+} or Cs^+ content, as a result of increased charging on the alkali cation.

Furthermore, the shoulders within this broad peak, at 1120 and 1160 cm^{-1}, represent more asymmetric stretching of specifically T–O–Si[1] and Si–O–Si,[29] respectively due to the bonds present in the aluminosilicate gel. This indicates the presence of unreacted metakaolin in the gel. The peaks below 900 cm^{-1} further confirm geopolymer formation, including: symmetric stretching of Al–O–Si (560 cm^{-1}),[29] the formation of a potassium substituted zeolite A, K-LTA (673 cm^{-1}),[30] symmetric stretching of T–O–T,[7] and the asymmetric stretching of T–O–T bonds linking AlO_4 and SiO_4 tetrahedral bonds,[1] respectively. The small peak at 810 cm^{-1} which is present on some samples could further indicate the formation of zeolitic material within these samples.[31] Finally, the peaks at 1300, 1370, 1470 cm^{-1} are consistent with the formation of carbonate ions of potassium/strontium/caesium.

A minor shift towards lower wavenumbers (by about 10 cm^{-1}) is observed due to the incorporation of Sr and Cs. This suggests that these cations enhance the charge-balancing capacity of the aluminosilicate gel, resulting in a higher proportion of Si–O–Al bonds compared with Si–O–Si bonds. This shifts the spectra towards lower wavenumbers and indicates that the cations are influencing the gel structure and therefore may be replacing the charge-balancing potassium cations.

Post-leach samples exhibit almost identical FTIR spectra, indicating there has been little observable change in the microstructure of the geopolymer gel during leaching. The main observable difference is that the carbonate peaks (red box included to indicate area where these peaks occur) are more intense in the post-leach samples than in the pre-leach samples, likely due to prolonged atmospheric exposure as these samples were not handled in an inert atmosphere.

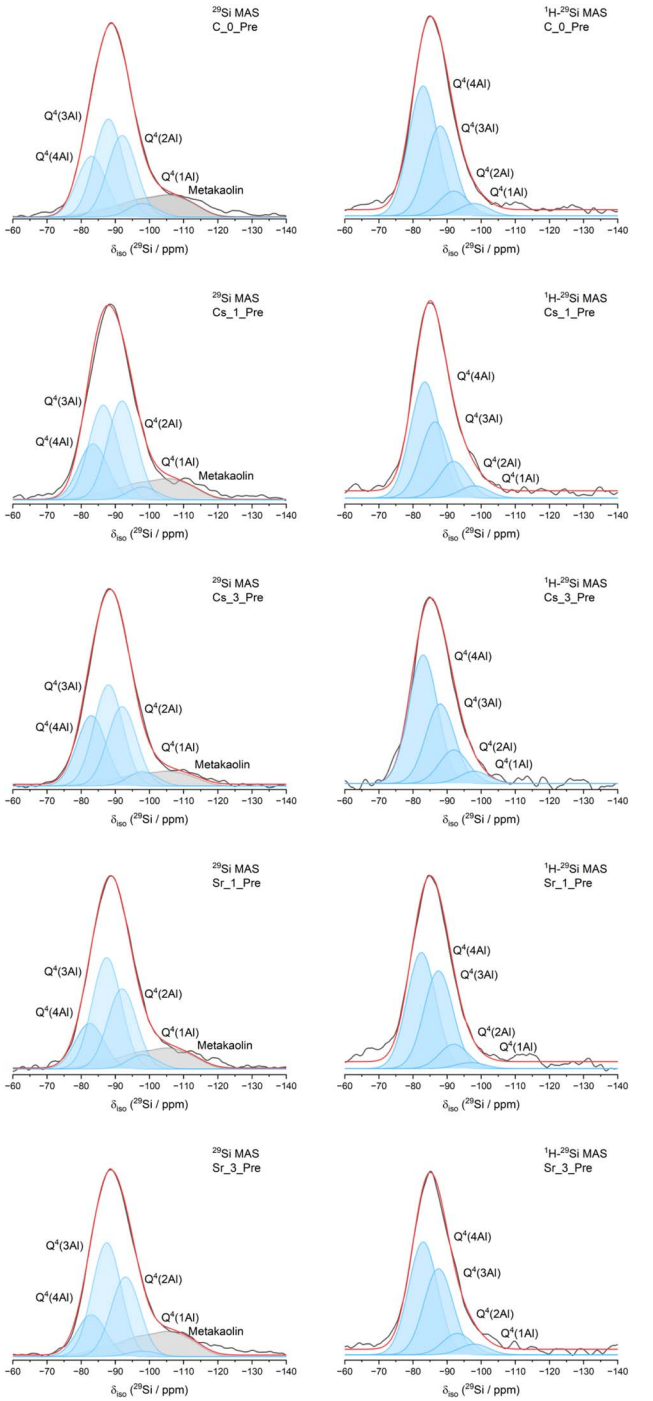

Fig. 7 ^{29}Si MAS ($B_0 = 11.7$ T, $\nu_R = 12.5$ kHz) and H–^{29}Si CPMAS ($B^0 = 11.7$ T, $\nu_R = 12.5$ kHz and Hartmann–Hahn contact period $t = 1.7$ ms) NMR spectra and associated deconvolutions for pre-leach geopolymer gels. The data are shown in black, the fit (the sum of the deconvoluted peaks) is shown in red, the peaks attributed to Si sites are shown in blue, and peaks attributed to Si sites in unreacted metakaolin in grey.

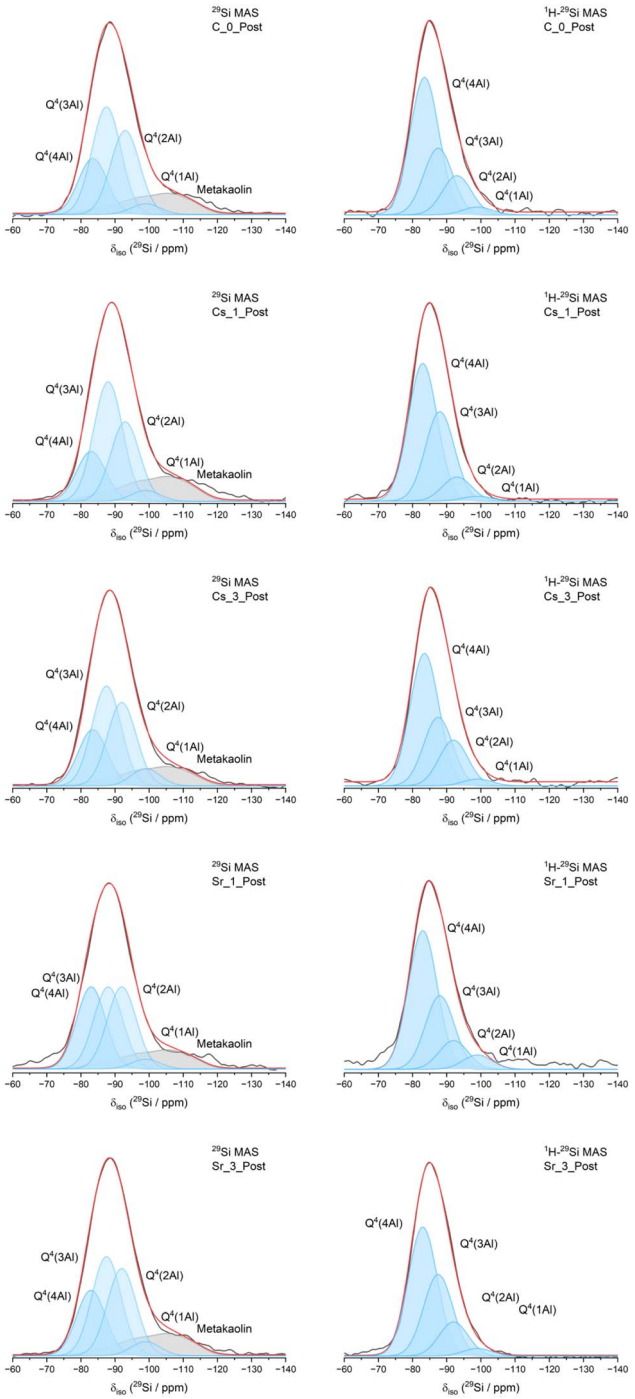

Fig. 8 ^{29}Si MAS ($B_0 = 11.7$ T, $\nu_R = 12.5$ kHz) and H–^{29}Si CPMAS ($B^0 = 11.7$ T, $\nu_R = 12.5$ kHz and Hartmann–Hahn contact period $t = 1.7$ ms) NMR spectra and associated deconvolutions for post-leach geopolymer gels. The data are shown in black, the fit (the sum of the deconvoluted peaks) is shown in red, the peaks attributed to Si sites are shown in blue, and peaks attributed to Si sites in unreacted metakaolin in grey.

4.2.4 Solid state nuclear magnetic resonance spectroscopy.

To further assess the effect on the nanostructure, ^{29}Si MAS, ^{1}H–^{29}Si CP MAS, and ^{27}Al MAS NMR data was acquired for all samples. The ^{29}Si MAS NMR and ^{1}H–^{29}Si CP MAS NMR spectra are shown in Fig. 6. The ^{29}Si MAS NMR data exhibit a maximum centred around $\delta_{iso} = -88.5$ ppm for the pre-leach samples and control and Cs post-leach samples, shifting to $\delta_{iso} = -89$ ppm for the Sr samples. As this is within the error of the instrument, this indicates no significant shift and therefore no significant changes in the bonding environments as a result of Cs and Sr incorporation or leaching. The ^{29}Si MAS NMR spectra exhibit a broad resonance spanning from $\delta_{iso} = -75$ ppm to 110 ppm with a consistent lineshape. The resonance indicates an extensive distribution of silicon environments consistent with the amorphous K–A–S–H gel indicated by FTIR and XRD. This contains contributions from a distribution of Q^4(mAl) environments where $0 \leq m \leq 4$.[1] As the maximum shift is at approximately $\delta_{iso} = -105$ ppm, this indicates the resonance is dominated by lower m values, indicating lower aluminium substitution.

To differentiate between the contributions from unreacted precursor (metakaolin) and the hydrated K–A–S–H gel, ^{1}H–^{29}Si cross polarisation MAS NMR spectra were collected which centred around $\delta_{iso} = -85$ ppm before and after leaching with all cation incorporation levels. The ^{1}H–^{29}Si cross polarisation MAS NMR spectra span from $\delta_{iso} = -75$ ppm to -95 ppm, all with a consistent lineshape. As the ^{1}H–^{29}Si cross polarisation MAS NMR signal is sensitive to internuclear distance between silicon atoms and nearby protons, the signal of silicon atoms near to protons is preferentially enhanced.[1] Therefore, it is possible to differentiate between the hydrated gel sites and the silicon sites in the metakaolin which remained unreacted and present in the geopolymer.

The deconvolutions for each NMR fit for pre- and post-leach samples are shown in Fig. 7 and 8, respectively with ^{29}Si MAS NMR on the left and ^{1}H–^{29}Si CP MAS NMR on the right for each sample. The deconvolution reveals five distinct silicon sites within the geopolymer sample at δ_{iso} values of -86 ppm, -90 ppm, 95 ppm, -102 ppm $\pm$ 4 ppm, and a broad resonance around -110 ppm.[32] These correspond to Q^4(4Al), Q^4(3Al), Q^4(2Al), and Q^4(1Al) in the K–A–S–H gel and Q^4(0Al) for the sites identified in the metakaolin precursor.[32] The sites present in the hydrated K–A–S–H gel were identified using the ^{1}H–^{29}Si CP MAS spectra.[32] These sites could then be quantified and compared with the unreacted metakaolin using the ^{29}Si MAS spectra.

For most samples, the Q^4(3Al) site is most abundant, followed by Q^4(2Al), then Q^4(4Al), with minor amounts of Q^4(1Al) and unreacted metakaolin. Sr incorporation into the

Table 5 Relative integral areas for silicon environments within K–A–S–H gel in each sample and associated Si/Al ratios

Site	Q^4(4Al)	Q^4(3Al)	Q^4(2Al)	Q^4(1Al)	Si/Al
C_0_Pre	23.9	38.6	32.1	5.4	1.42
Sr_1_Pre	18.2	44.3	31.8	5.7	1.45
Sr_3_Pre	17.3	47.4	33.1	2.3	1.43
Cs_1_Pre	21.3	36.1	37.7	4.9	1.46
Cs_3_Pre	26.5	38.1	29.9	5.4	1.40
C_0_Post	21.7	41.7	32.5	4.2	1.42
Sr_1_Post	32.1	32.1	32.1	3.8	1.37
Sr_3_Post	24.6	37.3	32.8	5.3	1.42
Cs_1_Post	19.2	46.0	30.5	4.2	1.43
Cs_3_Post	21.9	38.8	32.5	6.8	1.45

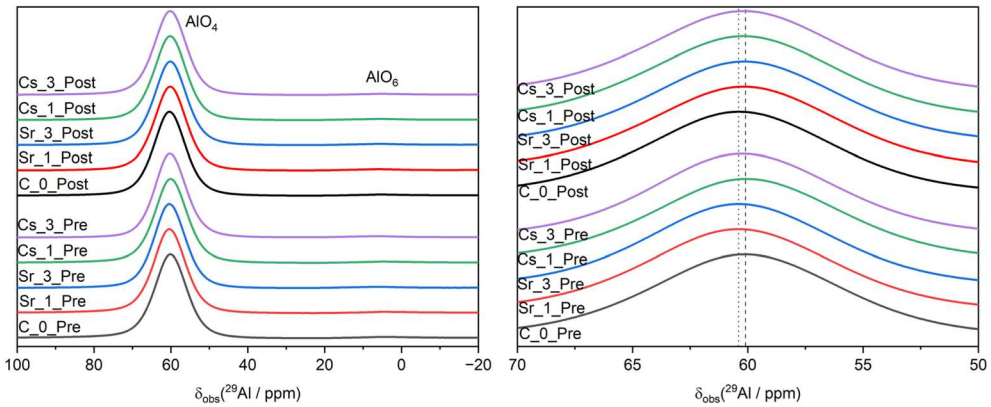

Fig. 9 ^{27}Al MAS NMR spectra ($B_0 = 11.7$ T, $\nu_R = 12.5$ kHz) for each geopolymer gel, pre- and post-leach, and for metakaolin.

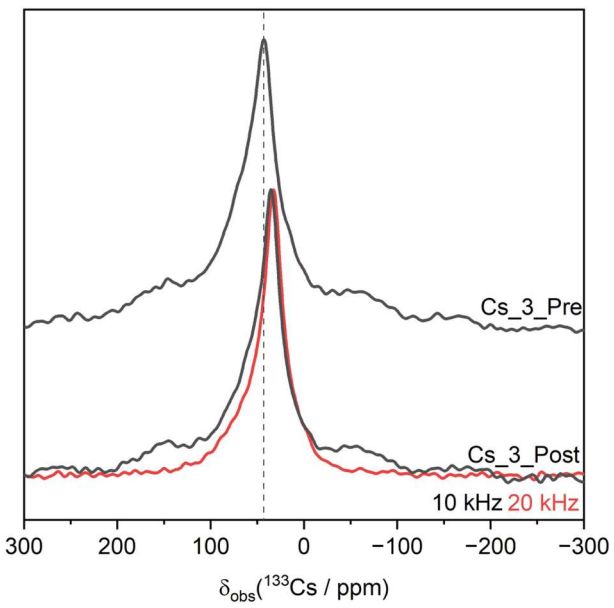

Fig. 10 ^{133}Cs MAS NMR spectra ($B_0 = 20.0$ T, $\nu_R = 10$ kHz (black) or $\nu_R = 20$ kHz (red)).

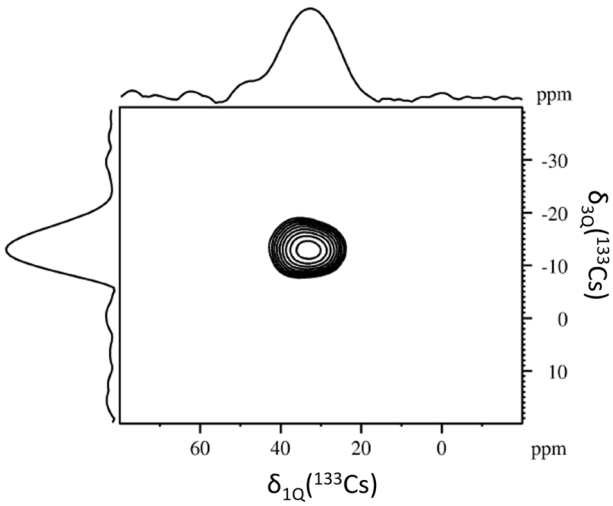

Fig. 11 ^{133}Cs MQMAS NMR spectra.

geopolymer increases Q^4(3Al) sites and reduces Q^4(4Al) sites, slightly increasing the Si/Al ratio.[33] Conversely, the effect of incorporating Cs is less consistent: at 1 wt%, Q^4(2Al) sites increase and dominate, but at 3 wt% Q^4(2Al) decreases while Q^4(4Al) increases, indicating unpredictable structural changes with more than one method of incorporation.

After leaching, the control sample shows a slight increase in Q^4(3Al) sites and a decrease in Q^4(4Al) sites, suggesting structural reordering into a less aluminium-rich gel, with a corresponding rise in the Si/Al ratio. This trend is also observed in the Cs samples at both 1 and 3 wt%. However, the Sr-containing samples exhibit the opposite trend, with an increase in Q^4(4Al) sites and a decrease in Q^4(3Al) sites (Table 5).

To assess the aluminium sites in the geopolymer matrix, ^{27}Al MAS NMR data were acquired and are plotted in Fig. 9. The main resonances due to aluminium at $\delta_{obs} = 56$, 33, and 8 ppm which are attributed to tetrahedral, pentahedral, and octahedral coordination.[1] All samples display one large resonance between $\delta_{obs} = 70$ and 50 ppm which is attributed to a AlO_4 structure within the K–A–S–H gel, indicating Al in within

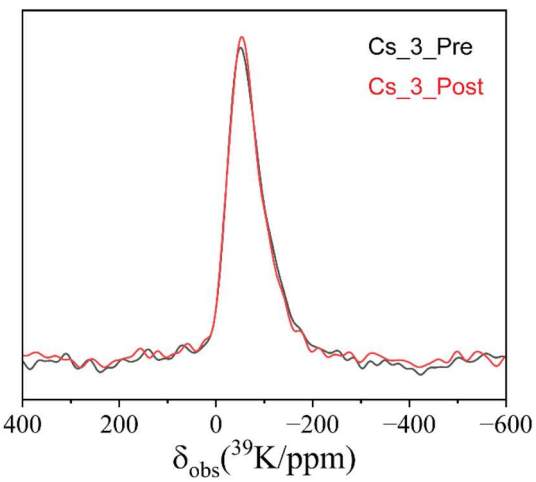

Fig. 12 ^{39}K MAS NMR spectra ($B_0 = 11.7$ T, $\nu_R = 12.5$ kHz) for the Cs_3 geopolymer gel, pre- and post-leaching.

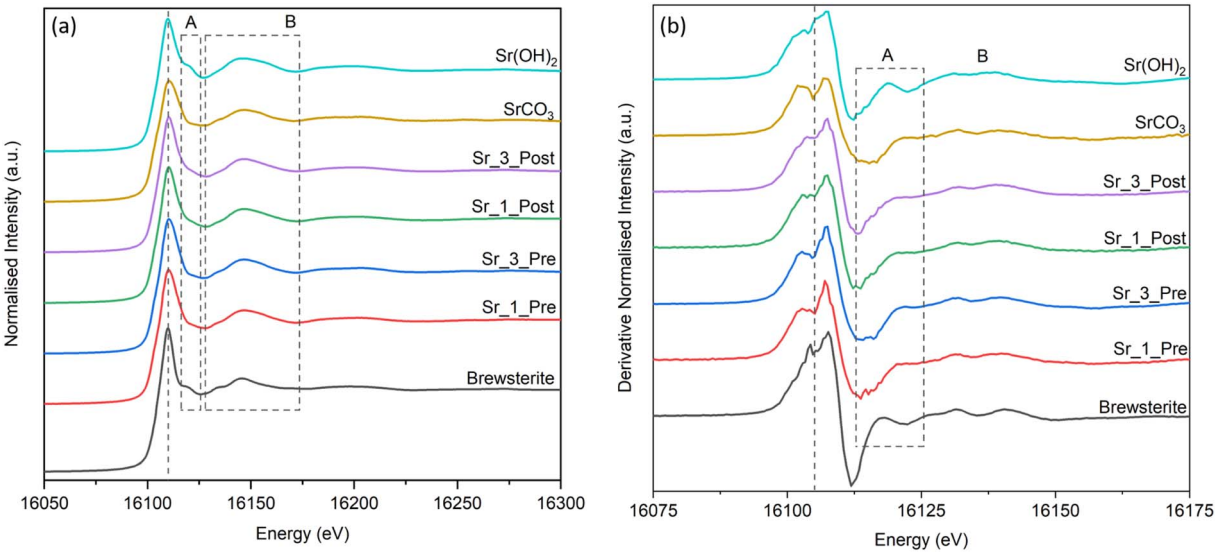

Fig. 13 (a) Normalised X-ray absorption spectra for the Sr-loaded geopolymer samples, brewsterite-Sr, and $SrCO_3$. (b) First derivative of the spectra.

a fully polymerised tetrahedral site. This is the expected coordination for aluminium to be in due to the excess of aluminium cations within the formulation of the cement.[1]

There is a very consistent lineshape with only a very small shift in the maxima (δ_{obs} = 60.0–60.5 ppm). In the pre-leach samples, the maxima are slightly higher for the Sr- containing samples than for the Cs or control samples ($\delta_{obs} \approx$ 60.5 ppm and 60.0 ppm, respectively), likely due to slight shielding of the ^{27}Al nucleus as a result of the divalent Sr^{2+} ion.[1] In the post-leach samples, this shielding is not observed to the same degree with the maxima for Sr being in line with that of Cs. This indicates there is some structural reordering during the leaching process, especially in the Sr containing samples. The negligible amount of AlO_6 and lack of AlO_5 coordination of aluminium for all samples and the lack of any other variation in the ^{27}Al MAS NMR spectra either after incorporation of cations or due to leaching indicates that there is little to no alteration in the local structure of the gel framework.

To further probe the environment of the Cs within the geopolymer gel, ^{133}Cs MAS data were acquired at the national high field facility in Warwick, UK, and is shown in Fig. 10. The black lines indicate samples which were spun at 10 kHz, in an attempt to improve the signal/noise ratio but this resulted in interference from the spinning side bands. Therefore, for the post-leach sample the sample spun at 20 kHz in a smaller rotor is also included in red, with less interference from spinning side bands.

The pre-leach sample has a symmetrical line-shape with a sharp peak and a broad base and is indicative of a Cs ion in a structure similar to that seen in zeolite-A,[18] with a chemical shift δ_{obs} = 42.7 (a line is included to guide the eye). This indicates that the Cs is bound into the charge-balancing sites of the aluminosilicate gel, in place of the K^+ ions in the K–A–S–H

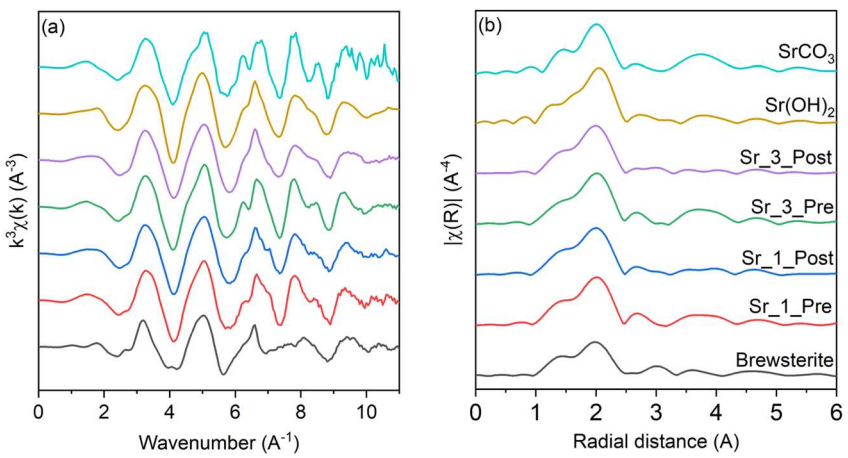

Fig. 14 (a) k^2 weighted $\chi(k)$ and (b) Fourier transforms (FT) of k^2-weighted $\chi(k)$ for the Sr-doped geopolymer and standard samples. The spectra have been stacked to improve clarity.

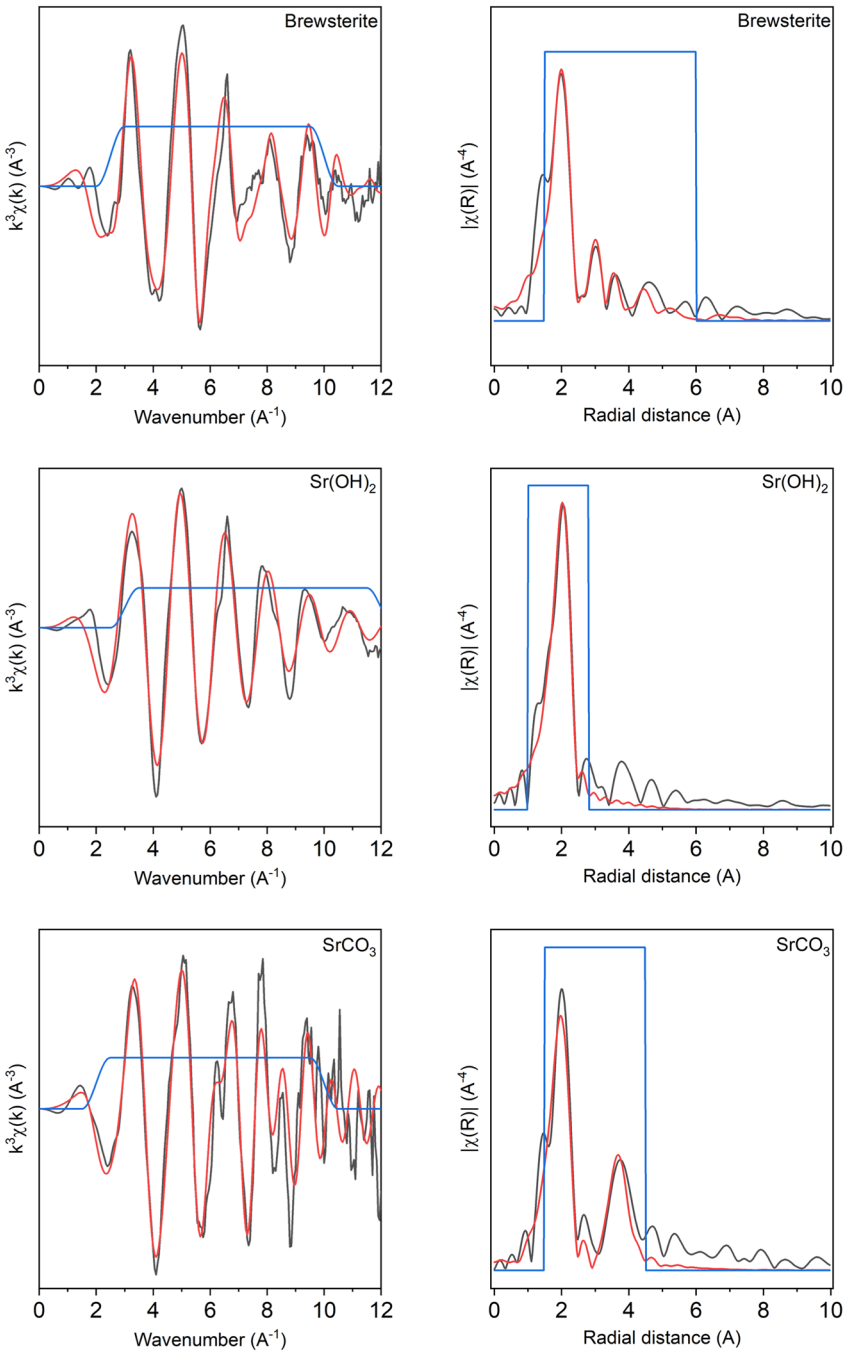

Fig. 15 $k^3\chi(k)$ and FT of $k^3\chi(k)$ for brewsterite, $Sr(OH)_2$, and $SrCO_3$. Solid black lines represent experimental data and solid red lines represent theoretical fits. Fitting windows are indicated by solid blue lines.

gel. However, there is a significant shift towards lower δ_{obs} values after leaching, with a chemical shift $\delta = 35.6$. This is more indicative of Cs in a zeolite-X structure,[34] which has a different shape to zeolite-A and offers larger pore sizes.[35] Furthermore, the peak becomes narrower after leaching, indicating that the Cs environment is more ordered or symmetric, possibly due to leaching of some of the loosely bound Cs causing some structural rearrangement. The ^{133}Cs data for the sample spun at 20 kHz confirms that the Cs is present in only one site.

^{133}Cs multiple-quantum magic angle spinning (MQMAS) data of the post-leach, 3% sample, is in Fig. 11. MQMAS is a powerful technique which can study half-integer quadrupolar nuclear (such as ^{133}Cs which has $I = \frac{7}{2}$).[36] The two-dimensional plot allows resolution of overlapping sites by separating quadrupolar broadening effects.[36] The spectrum shows a single, well-defined peak which confirms the presence of a single Cs site, or potentially two very similar overlapping Cs sites, with a relatively symmetrical local environment. This, combined with the insights from the ^{133}Cs MAS NMR, confirms that Cs is likely

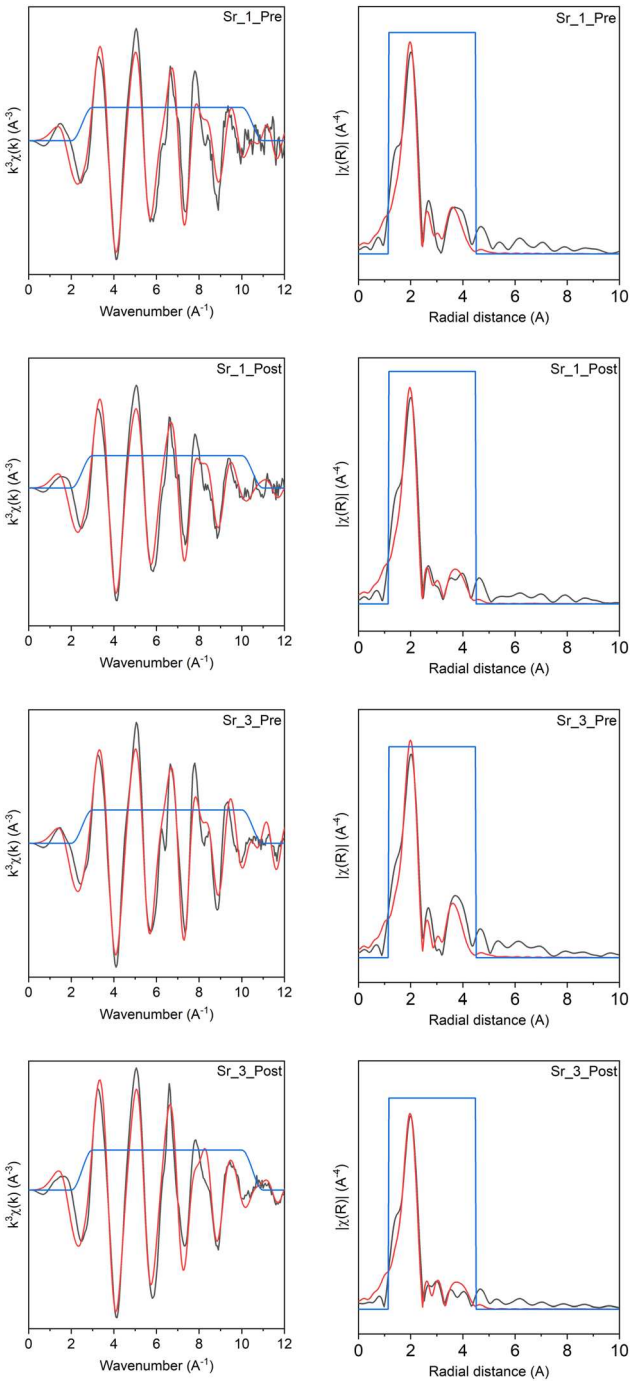

Fig. 16 $k^3\chi(k)$ and FT of $k^3\chi(k)$ for pre- and post-leach Sr samples. Solid black lines represent experimental data and solid red lines represent theoretical fits. Fitting windows are indicated by solid blue lines.

only present in a zeolitic structure, as discussed in Section 4.1 and corroborated by the ^{133}Cs spectrum for the sample spun at 20 kHz, and is not forming any significantly different sites.

High field 39 K MAS NMR data (Fig. 12) were obtained for the Cs_3 samples before and after leaching. The data exhibit a broad resonance spanning from $\delta_{obs} = 20$ ppm to -300 ppm, centred at $\delta_{obs} = -53$ ppm. This indicates charge-balancing extra-framework K^+ ions within a (N,K)–A–S–H-type gel.[33] The width and lineshape of the chemical shift distribution in the ^{39}K MAS NMR data is very similar for the sample before and after leaching, indicating no significant changes to the local environment of K.

4.2.5 X-ray absorption spectroscopy. XAS can be used as a diagnostic tool to probe the local structure of Sr within the sample. Fig. 13 shows the normalised Sr K-edge X-ray absorption spectra for the samples, which can assess the effect of Sr loading and leaching on the chemical immobilisation of the Sr. Cs is omitted from this technique due to edge overlap with titanium, an impurity in the metakaolin precursor, which has made data acquisition unreliable due to excessive noise. Previous work[33] has shown that Sr coordination in unreacted geopolymer cement samples is similar to that seen in $SrCO_3$, $Sr(OH)_2$, and/or brewsterite-Sr (a zeolitic mineral with the nominal composition of $(Sr,Ba)_2Al_4Si_{12}O_{32}\cdot 10H_2O$), of which data are overlaid for comparison.

The Sr K-edge is characterised by a smoothly rising absorption edge with a single peak at the maximum. A line is included to guide the eye. Although the absorption edge appears relatively featureless, when displayed in normalised intensity (Fig. 13b) the visibility of subtle features is enhanced. There is a slight shift in the peak of the brewsterite first derivative compared to the samples and the $SrCO_3$ or $Sr(OH)_2$. Close inspection reveals a doublet in the peak, the relative intensity of which changes between samples and reference standards. The brewsterite derivative spectrum reveals a doublet with two sharp features, the $SrCO_3$ reveals a doublet with two broad peaks, and the $Sr(OH)_2$ reveals a doublet with one shallow peak and one broad peak. The pre-leach samples have a shallow peak and then a sharp peak, with the post-leach revealing a slightly less intense first peak. One feature (feature A) on Fig. 13a shows a shoulder on the brewsterite-Sr and $Sr(OH)_2$ which is not clearly visible on the $SrCO_3$ or the sample spectra. This is clearer in the derivative plot, where there is a clear, broad peak indicated by the box. The final feature (feature B), present on all samples, is slightly sharper for the brewsterite-Sr.

Direct visual comparison of the samples with the standards can indicate the coordination of the Sr within the geopolymer matrix. The pre-leach spectra are visually similar to the local structure of Sr is in a zeolitic structure, such as brewsterite-Sr, as well as $SrCO_3$. However, the direct visual comparison of those samples with the post-leach samples does reveal some slight changes in the spectra which could indicate a change in the Sr local structure, towards a mixture of zeolitic and $SrCO_3$/$Sr(OH)_2$-type local structures.

4.2.5.1 Extended X-ray absorption fine structure (EXAFS). EXAFS can determine the local coordination environment of the Sr in the geopolymer samples before and after leaching. Fig. 14a shows the k^3-weighted EXAFS oscillations and Fig. 14b shows the magnitude of the Fourier transform (FT), which allows a direct, phase-shifted view of the radial structure. Also included are reference spectra for brewsterite, $Sr(OH)_2$, and $SrCO_3$ for comparison.

Visual inspection of Fig. 14 reveal similarities between the spectra and those of brewsterite (a monoclinic zeolite with formula $(Sr,Ba)_2Al_4Si_{12}O_{32}\cdot 10H_2O$), $SrCO_3$, and $Sr(OH)_2$. This

Table 6 Structural parameters derived for the Sr K-edge EXAFS of the pre- and post-leach using the brewsterite standard. $R_{Sr\text{-}i}$ represents the average interatomic distance to the absorbing atom (Sr), σ^2 represents the Debye–Weller factor, and $N_{Sr\text{-}i}$ represents the coordination number. The amplitude reduction factor (S_0^2) was set to 1.0

Sample	*R*-factor	ΔE_0	±	$R_{Sr\text{-}i}$	±	σ^2	±	$N_{Sr\text{-}i}$	±
Sr_1_Pre	0.035	−4.33	1.52	—	—	—	—	—	—
Sr–O_1	—	—	—	2.58	0.058	0.013	0.0011	9.0	
Sr–Si	—	—	—	3.73	0.088	0.024	0.013	4.5	
Sr–Al	—	—	—	4.09	0.012	0.0039	0.0063	1.5	
Sr–O_2	—	—	—	4.65	0.018	0.013	0.0011	8.0	
Sr_1_Post	0.035	−4.18	1.59	—	—	—	—	—	—
Sr–O_1	—	—	—	2.57	0.16	0.013	0.0011	9.0	
Sr–Si	—	—	—	3.77	0.012	0.020	0.0083	4.0	
Sr–Al	—	—	—	4.09	0.0087	0.0098	0.0091	2.0	
Sr–O_2	—	—	—	4.63	0.00002	0.013	0.0011	8.0	
Sr_3_Pre	0.029	−3.83	1.22	—	—	—	—	—	—
Sr–O_1	—	—	—	2.59	0.15	0.011	0.00090	9.0	
Sr–Si	—	—	—	3.78	0.14	0.020	0.0074	4.0	
Sr–Al	—	—	—	4.10	0.0017	0.0036	0.0034	2.0	
Sr–O2	—	—	—	4.66	0.027	0.011	0.00090	8.0	
Sr_3_Post	0.030	−3.70	1.31	—	—	—	—	—	—
Sr–O_1	—	—	—	2.58	0.16	0.013	0.0010	9.0	
Sr–Si	—	—	—	3.78	0.14	0.013	0.00059	3.0	
Sr–Al	—	—	—	4.09	0.0087	0.0098	0.0091	3.0	
Sr–O_2	—	—	—	4.67	0.041	0.013	0.0010	8.0	

suggests the Sr may occupy multiple local environments within the sample.

The amplitude reduction factor (S_0^2) was determined by fitting FEFF-generated structural models of both brewsterite and $SrCO_3$ to the experimental standard data. A value of $S_0^2 = 1$ was satisfactory and was subsequently used for all sample refinements. The brewsterite model included single scatter paths for nearest-neighbour O, Si, and Al atoms. The $SrCO_3$ model consisted of nearest-neighbour O shell ($N = 9$), and two further out cation shells ($N = 6$). Fig. 15 shows the fits to the structural models for the standards. Given the similarities observed between the samples and brewsterite, the Sr K-edge EXAFS data for the samples were modelled using the brewsterite model. Attempts to fit the samples using the $SrCO_3$ and $Sr(OH)_2$ models resulted in poor fits and were discarded.

For all samples, the following fitting approach was used:

- S_0^2 was fixed at 1 based on the standard refinements.
- Path degeneracies (N) were fixed according to the refined brewsterite structure.
- All Debye–Waller factors (σ^2) were restrained by element type.
- Multiple single-scatter O paths at similar distances were combined into an effective path.

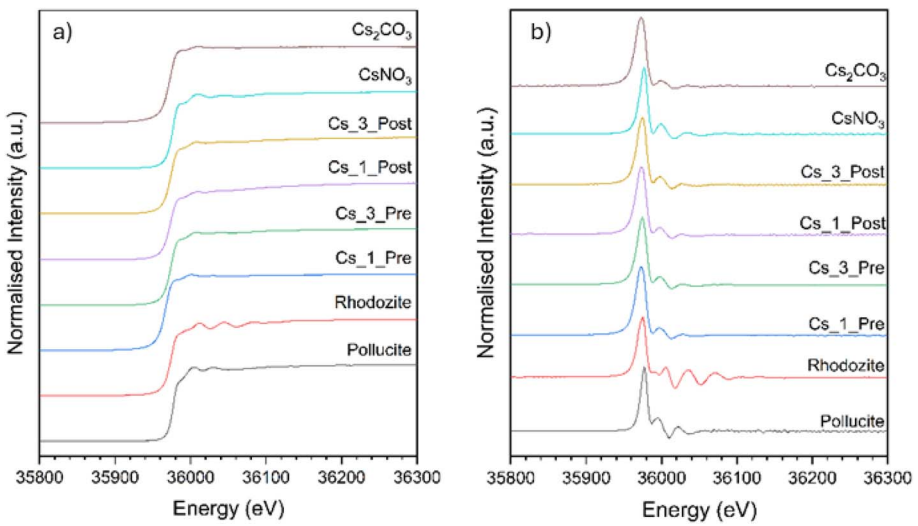

Fig. 17 (a) Normalised X-ray absorption spectra of Cs-loaded geopolymer samples, Cs_2CO_3, $CsNO_3$, Cs-rhodozite, and Cs-pollucite. (b) First derivative of the spectra.

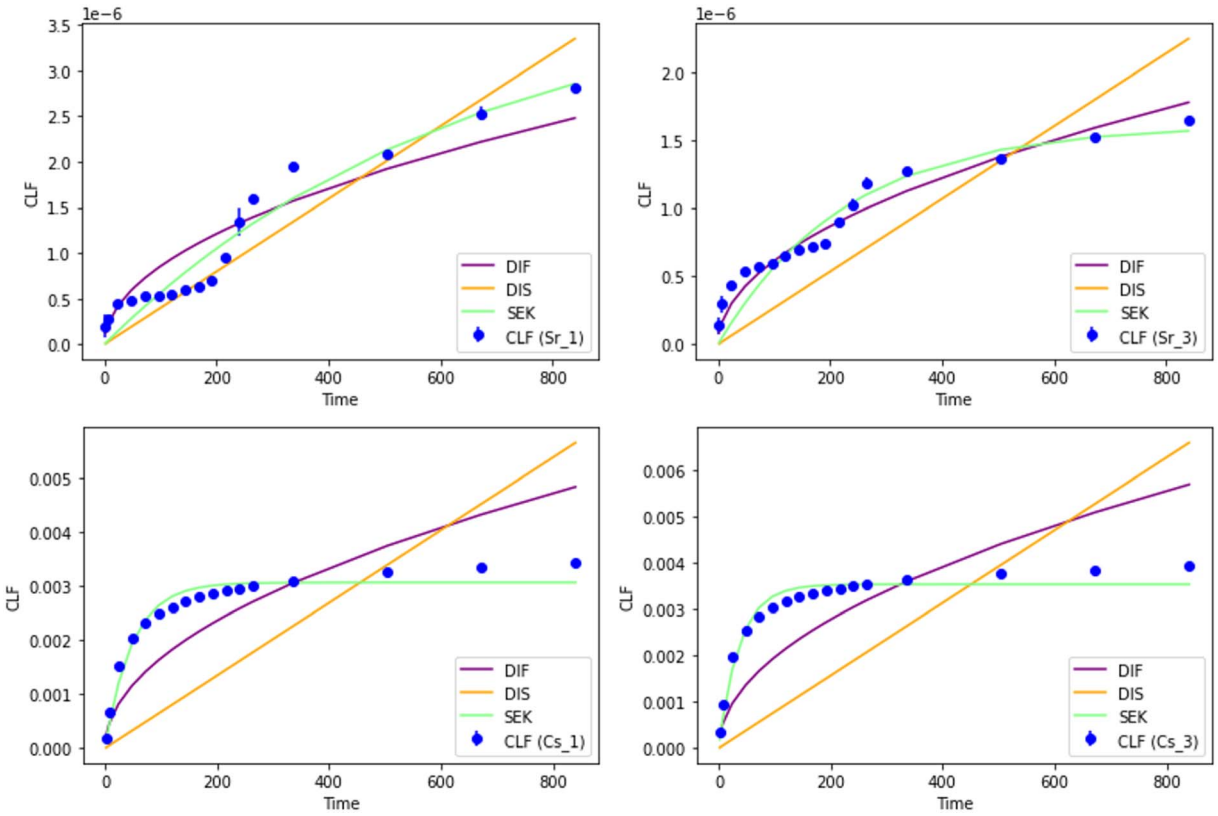

Fig. 18 Single source mass transfer models for (top) Sr and (bottom) Cs. Experimental data is plotted as blue dots, models are plotted as lines (DIF = diffusive, DIS = dissolutive, SEK = surface exchange kinetics.).

• The Si/Al ratio was set to the ratio defined in the experiment, but due to CIF and FEFF restrictions of no mixed occupancy sites, this is not a perfect, realistic representation of the system.

Although the overall fits are good, it is acknowledged that the mismatch between the modelled and real Si/Al distribution is likely introducing uncertainty, leading to large uncertainties on the Al paths. This reflects static disorder from the random distribution of Al and Si on the same crystallographic sites, which cannot be fully modelled by FEFF.

Table 7 Associated variables for each single-source mass transport model as calculated from `scipy.optimize.curve_fit` in Python

	Model	Variable	R^2
Sr_1	DIF	$D = 1.88 \times 10^{-17} \pm 2.1 \times 10^{-18}$	0.872
	DIS	$U = 2.28 \times 10^{-10} \pm 1.3 \times 10^{-11}$	0.893
	SEK	$C = 3.91 \times 10^{-6} \pm 7.0 \times 10^{-7}$	0.938
		$k = 0.00156 \pm 0.00042$	
Sr_3	DIF	$D = 9.70 \times 10^{-18} \pm 5.0 \times 10^{-19}$	0.950
	DIS	$U = 1.53 \times 10^{-10} \pm 1.5 \times 10^{-11}$	0.594
	SEK	$C = 1.61 \times 10^{-6} \pm 1.2 \times 10^{-7}$	0.912
		$k = 0.00433 \pm 0.00068$	
Cs_1	DIF	$D = 7.18 \times 10^{-11} \pm 9.9 \times 10^{-12}$	0.467
	DIS	$U = 3.86 \times 10^{-7} \pm 6.4 \times 10^{-8}$	0.467
	SEK	$C = 0.00307 \pm 7.0 \times 10^{-5}$	0.956
		$k = 0.0207 \pm 0.0023$	
Cs_3	DIF	$D = 9.92 \times 10^{-11} \pm 1.5 \times 10^{-11}$	0.270
	DIS	$U = 4.49 \times 10^{-7} \pm 7.8 \times 10^{-8}$	−0.981
	SEK	$C = 0.00354 \pm 7.3 \times 10^{-5}$	0.953
		$k = 0.0270 \pm 0.0032$	

The resulting fits are shown in Fig. 16 and the calculated factors in Table 6.

For the Sr_1_Pre sample, the best fit was obtained by representing inner shell O paths as a single oxygen path at 2.58 Å (N = 9). A Sr–Si path with a scattering length of 3.73 Å and a Sr–Al path with a scattering length of 4.09 Å, adjusted to 3 : 1 to reflect the realistic composition, were added. Finally, as with the inner shell, the outer shell oxygens best fit was obtained where all single scatter oxygen paths were represented by a single path at 4.65 Å, providing an overall satisfactory fit.

However, in Sr_1_Post, although the scattering lengths are very similar to the Sr_1_Pre sample, with inner shell O, Sr–Si, Sr–Al, and outer shell O scattering lengths of 2.57, 3.77, 4.09, and 4.63 Å, respectively, the Al/Si ratio adjustments were required for a satisfactory fit to be achieved. Overall, the Sr_1_Post sample showed a similar fit to Sr_1_Pre, with slight structural changes as the Sr–Si and Sr–Al contributions alter slightly.

Although still satisfactory, the fits for the samples with 3% loading were slightly inferior, indicated by the larger errors on the Sr–O and Sr–Si distances. Alternative inner shell oxygen paths were attempted, however the best fit was still achieved around the 2.58 Å distance, indicating that the local structure around the Sr absorber is similar to Sr_1_Pre. The larger errors, however, may indicate subtle differences in the long-range

Table 8 Model fit details as calculated from 'scipy.optimize.differential_evolution' package

Sample	Model	Parameters	R^2
Sr_1	DSEM	$D = 0.0 \pm 7.8 \times 10^{-18}$ $C = 3.90 \times 10^{-6} \pm 1.1 \times 10^{-6}$ $k = 0.00156 \pm 0.062$	0.937
	DDM	$D = 0.0 \pm 5.5 \times 10^{-18}$ $U = 2.28 \times 10^{-10} \pm 3.2 \times 10^{-11}$	0.860
	DISEM	$U = 1.90 \times 10^{-10} \pm 2.7 \times 10^{-7}$ $C = 3.02 \times 10^{-7} \pm 2.2 \times 10^{-7}$ $k = 0.483 \pm 0.36$	0.928
Sr_3	DSEM	$D = 0.0 \pm 0.0$ $C = 1.61 \times 10^{-6} \pm 1.1 \times 10^{-7}$ $k = 0.00434 \pm 0.000876$	0.900
	DDM	$D = 0.0 \pm 0.0$ $U = 1.53 \times 10^{-10} \pm 2.6 \times 10^{-11}$	0.318
	DISEM	$U = 8.69 \times 10^{-11} \pm 1.3 \times 10^{-11}$ $C = 5.31 \times 10^{-7} \pm 1.1 \times 10^{-7}$ $k = 0.0872 \pm 0.30$	0.930
Cs_1	DSEM	$D = 5.05 \times 10^{-12} \pm 1.5 \times 10^{-12}$ $C = 0.00223 \pm 9.25 \times 10^{-5}$ $k = 0.0331 \pm 0.0032$	0.996
	DDM	$D = 7.22 \times 10^{-11} \pm 1.3 \times 10^{-11}$ $U = 1.51 \times 10^{-10} \pm 7.08 \times 10^{-11}$	0.379
	DISEM	$U = 6.05 \times 10^{-8} \pm 2.3 \times 10^{-8}$ $C = 0.00265 \pm 0.000254$ $k = 0.0304 \pm 0.29$	0.992
Cs_3	DSEM	$D = 5.26 \times 10^{-12} \pm 2.22 \times 10^{-12}$ $C = 0.00272 \pm 0.000124$ $k = 0.0417 \pm 0.0054$	0.994
	DDM	$D = 9.88 \times 10^{-11} \pm 2.10 \times 10^{-11}$ $U = 3.94 \times 10^{-12} \pm 8.0 \times 10^{-11}$	0.134
	DISEM	$U = 6.18 \times 10^{-8} \pm 2.7 \times 10^{-8}$ $C = 0.00314 \pm 0.00026$ $k = 0.0378 \pm 0.25$	0.988

Table 9 R^2 values for the split models

Sample	Model	R^2 < 200 h	R^2 > 200 h
Sr_1	DIF	0.630	0.901
	DIS	−0.198	0.630
	SEK	0.777	0.0
	DSEM	0.774	0.936
	DDM	−0.762	0.561
	DISEM	0.966	0.936
Sr_3	DIF	0.821	0.802
	DIS	0.202	−0.966
	SEK	0.886	0.0
	DSEM	0.882	0.942
	DDM	−0.137	−1.45
	DISEM	0.994	0.949

structure or larger contribution from other structures, such as $Sr(OH)_2$ or $SrCO_3$. For the Sr_3_Pre sample, the Sr–Si, Sr–Al, and outer shell O paths were 3.78, 4.10, and 4.66 Å, respectively. For the Sr_3_Post sample, the Sr–Si, Sr–Al, and outer shell O paths were 3.78, 4.09, and 4.67 Å, respectively. Both these fits are very similar to the 1% loaded samples, which minimal changes in the bond scattering lengths. However, again the Si/Al ratio had to be adjusted for a satisfactory fit.

Across all samples, the first-shell Sr–O distance (2.57–2.59 Å) and coordination number ($N = 9$) remains unchanged before and after leaching, indicating that the immediate Sr–O environment is preserved. However, small changes in the other shell contributions reveal:

• At low Sr loading (1%), the change in the Sr–Si and Sr–Al contributions are relatively minimal after leaching.

• At higher Sr loading (3%), N_{Sr-Si} decreases from 4 to 3 after leaching, while N_{Si-Al} increases from 2 to 3. This suggests that the local environment around the Sr absorber may be altering slightly, potentially towards a carbonate or hydroxide environment or due to the partial crystallisation of the amorphous gel, as discussed in Section 4.1. However, this is not a significant enough change to cause a large interference with the brewsterite EXAFS signal.

Overall, the EXAFS analysis indicates that a brewsterite-based structural model adequately described Sr coordination, before and after leaching. At higher Sr loadings, slightly inferior model fits indicate partial Sr relocation or precipitation into secondary phases such as carbonate, hydroxide, or re-absorption into a crystalline zeolite site, however this is very minimal. The small structural changes are consistent with the low leaching rates of Sr and somewhat explain the distinct, 'S-shaped' curve.

Multi-phase EXAFS fits were attempted, combining brewsterite and $SrCO_3$ models, but these could not be successfully fit. However, the single-model fits using brewsterite, combined with the other solid-state characterisation techniques, provide confidence in the precipitation of some level of Sr to $SrCO_3$ at high waste loadings and the potential crystallisation of the amorphous gel.

4.2.5.2 Cs K-edge X-ray absorption near edge fine structure (XANES). XANES can be utilised to infer the local coordination of Cs within geopolymer samples before and after leaching. Fig. 17 shows the Cs–K edge XANES spectra for geopolymer samples with comparative standards.

Visual inspection of XANES and derivative plots showed significant similarity between loaded geopolymers before and after leaching experiments with minimal changes in post-edge features, particularly the features at 36 000 eV and 36 025 eV which are present in all loaded geopolymer samples. Intensity and positions of both post-edge features remain consistent between pre and post leaching samples, indicating negligible change in the immediate coordination environment of the Cs.

Comparison with standards of Cs_2CO_3, and $CsNO_3$ show similar features to loaded geopolymers with oscillations also at 36 000 eV and 36 025 eV with no discernible oscillations thereafter.

The lack of further post-edge oscillations in geopolymer samples is indicative of low-crystallinity or amorphous coordination environments around the Cs absorber, with Cs_2CO_3 and $CsNO_3$ standards also showing low intensity oscillations after the absorption edge, likely as a result of deliquescence leading to poor crystallinity. This contrasts with the more crystalline Rhodozite and Pollucite samples which display more intense oscillations beyond the absorption edge.

4.3 Leaching characteristics

4.3.1 Single source mass transport models. To identify the dominant release mechanisms of Cs and Sr from the geopolymer

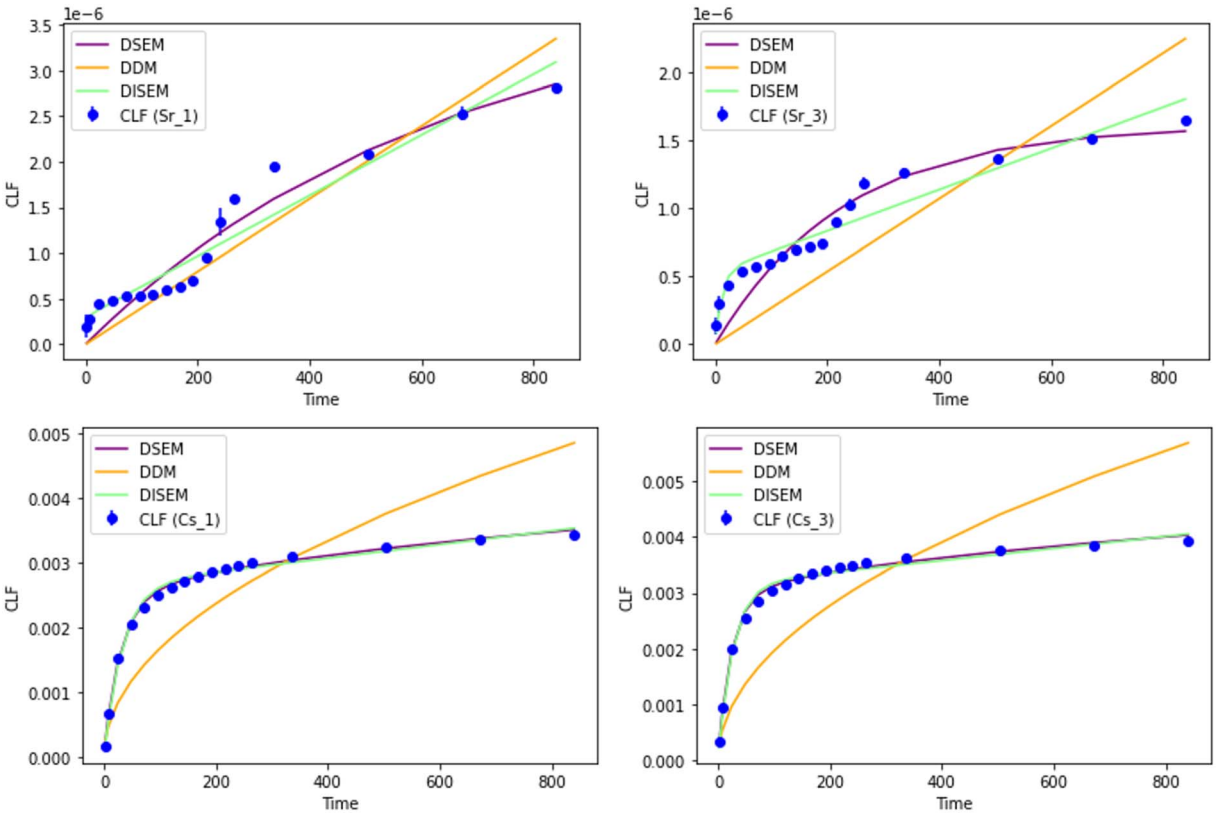

Fig. 19 Combined source mass transfer models for (top) Sr and (bottom) Cs. Experimental data is plotted as blue dots, models are plotted as lines.

matrix, conceptual models based on established mass transport mechanisms were developed and compared to the experimental CFL for each sample. These models (detailed in Section 3) were fitted to the experimental data using Python's `scipy.optimize.curve_fit` function. Goodness of fit was evaluated using R^2 values. Fig. 18 illustrates the fits, with corresponding parameters and R^2 values summarised in Table 7. Optimal model fits are characterised by the R^2 approaching one.

The models represent diffusion (DIF), dissolution (DIS), and surface-exchange kinetics (SEK), or reaction. The diffusion model assumes that the Sr or Cs is initially distributed evenly throughout the sample and then diffuses through the pores. The dissolution model assumes that the Sr or Cs is a major structural component of the geopolymer matrix and therefore its release causes a breakdown in the structure. Finally, surface exchange kinetics, or reaction, models the release of the Sr or Cs which is readily soluble at the surface of the geopolymer. This is also sometimes known as surface wash-off.[10]

For Sr at the lower loading concentrations (1%), diffusion (DIF), dissolution (DIS), and surface exchange kinetics (SEK) models all demonstrated reasonable fits to the experimental CFL data ($R^2 > 0.85$). SEK yields the highest R^2 value, indicating that surface exchange kinetics primarily govern the release. The non-negligible contributions from DIF and DIS also indicate more complex changes at the material surface. As described previously, it is hypothesised that the recrystallisation of an initially amorphous secondary alteration phase (*e.g.* K–A–S–H gel to zeolite) led to a resumption in the release of Sr^{2+} into solution after 200 hours.

At higher Sr waste loadings (3%), DIF and SEK models exhibited strong correlation with the experimental data ($R^2 > 0.90$). However, DIS demonstrated poor agreement ($R^2 = 0.59$), indicating less contribution from dissolutive processes. This observation suggests that higher Sr loadings favour diffusion-controlled release, as more loosely bound Sr is available, relative to the more structural Sr. This may be because, at higher waste loadings, there is a greater proportion of $SrCO_3$ or $Sr(OH)_2$ compared with structurally bound, zeolitic Sr, allowing it to diffuse more readily rather than relying on dissolution or reactive processes for release.

Cs release was primarily governed by the SEK model ($R^2 > 0.95$), while DIF and DIS show very poor correlation with the experimental data. The Cs experimental release exhibits a rapid initial wash-off phase, followed by a plateau after ~200 hours, suggesting there are two distinct release phases. The DIF model under-predicts the initial release and over-predicts the later release, whereas the DIS model fails to describe the release behaviour at any stage. The SEK model accurately predicts the first 300 hours, but under-predicts thereafter.

Overall, the observed contributions from multiple release mechanisms suggests that the release of Sr and Cs from the studied geopolymer wasteform involves a complex interplay of interacting processes.

4.3.2 Combined source mass transport models. To validate the contribution of multiple mass transport mechanisms to the release of Cs and Sr from the geopolymers, the models described in Section 3 were superimposed and fitted to the experimental releases. This optimisation was performed using Python's `'scipy.optimize.differential_evolution'` function, an algorithm designed to calculate the global maximum which is particularly effective for models with multiple parameters, compared to `'scipy.optimize.curve_fit'`. Goodness of fit was evaluated using R^2 values with the results and calculated model parameters summarised in Table 8.

For the Cs-containing samples, the DSEM and DISEM models accurately predict the release behaviour across the entire dataset. In conjunction with observations from the single-source models, these results suggest that surface exchange kinetics are the dominant release mechanism for Cs release, with diffusion contributing at later time points.

For Sr, the superimposed models provide a significantly improved representation of the experimental data compared to the single-source models, with most fits achieving high R^2 values, with the exception of the DDM model for the 3% loaded sample. This observation confirms the complex, multi-parametric nature of Sr mass transport, which cannot be accurately described by a single release mechanism.

Despite achieving high R^2 values, the combined models were still unable to accurately predict the S-shaped release profile observed in the experimental data. This could be attributed to a 'rate resumption' effect analogous to glass systems, as described in Section 4.1. Specifically, due to the crystallisation of the K–A–S–H gel to a zeolitic structure, evidenced by the presence of zeolitic phases in both NMR and XAS, could influence the Sr mobility. Potentially, the Sr is well incorporated into the amorphous gel but only partially within the crystalline zeolite, causing the Sr to be 'kicked out' of the structure as precipitation occurs.

The rate resumption period is more pronounced in the 1% samples, further indicating that diffusion dominates throughout the entire leaching process for the 3% sample. A possible explanation is that, at 1% loading, a greater proportion of Sr is bound into the amorphous gel, whereas at 3% loading, potential saturation of Sr into more stable $SrCO_3$ which remains unaffected by the crystallisation of the gel into zeolite.

Another plausible explanation is the presence of two distinct mass transport phases: an initial phase dominated by diffusion of loosely bound ions, followed by a period dominated by structural effects. To accurately model the two distinct mass transport phases, the experimental data was truncated into time points before 200 hours and after 200 hours, and then fitted to both single-source (Fig. 20) and combined source (Fig. 21) models. The corresponding R^2 values are presented in Table 9.

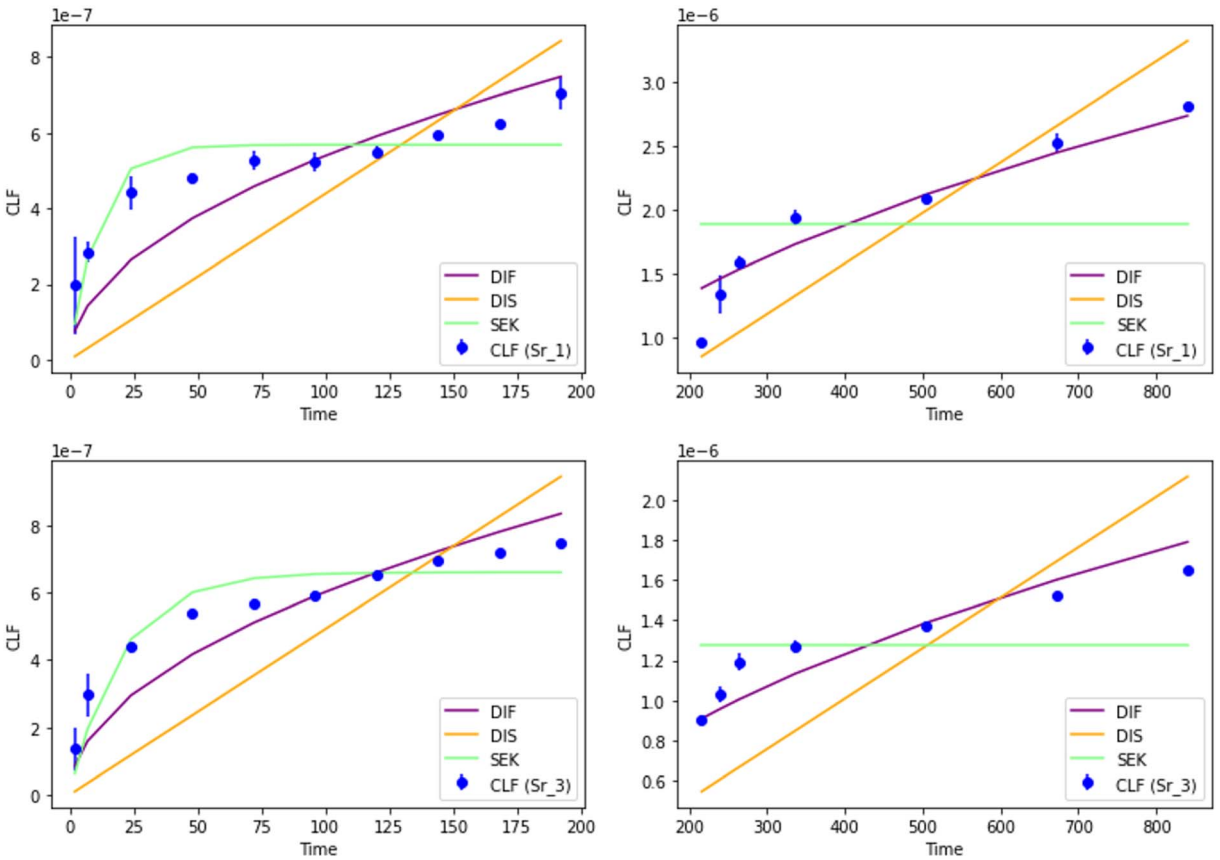

Fig. 20 Single-source mass transport model fits for Sr at 1% (top) and 3% (bottom) waste loading. The plots are split into prior to 200 hours and after 200 hours.

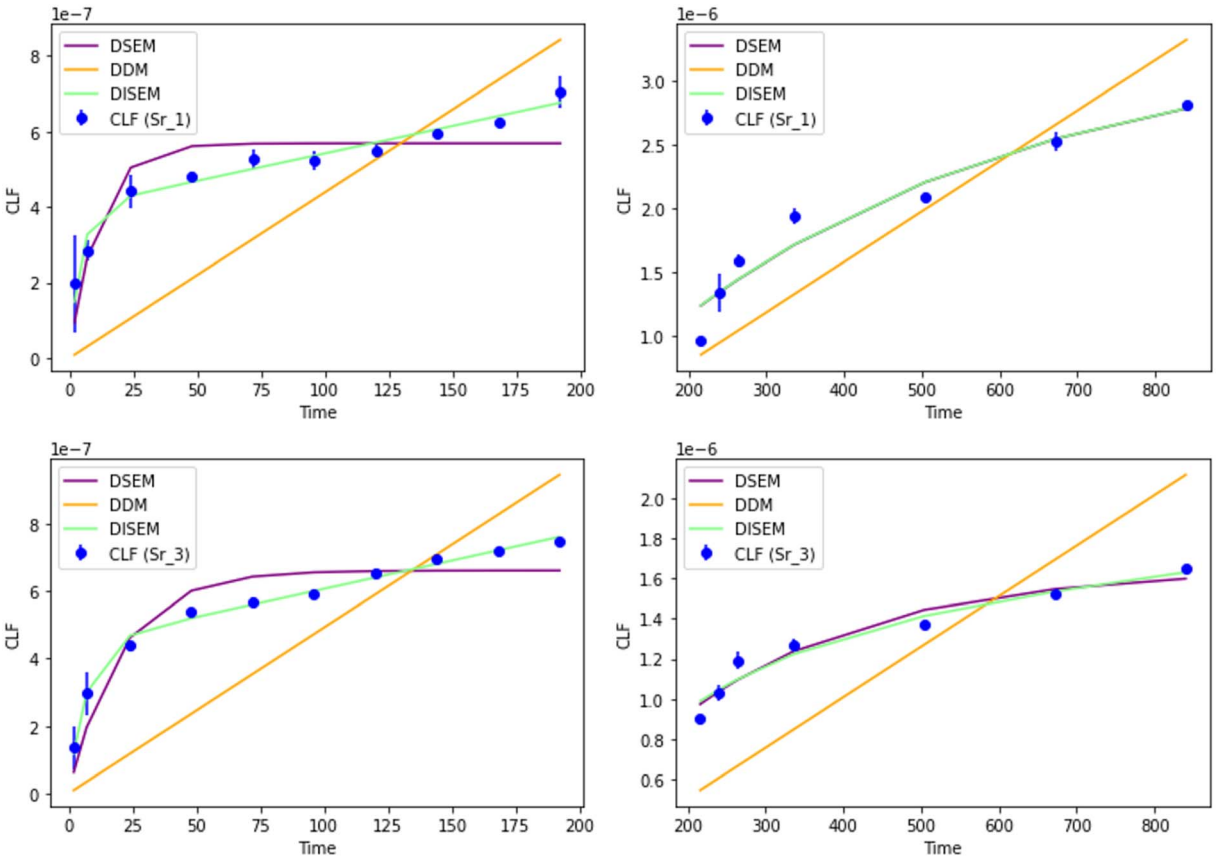

Fig. 21 Combined-source mass transport model fits for Sr at 1% (top) and 3% (bottom) waste loading. The plots are split into prior to 200 hours and after 200 hours.

Visual inspection of the model fits revealed no substantial improvement when the data was segmented. Across both time intervals, the DSEM and DISEM models consistently show the most agreement with the experimental release data, yielding high R^2 values.

The lack of improvement in fit with the truncated data indicates that it is not two distinct phases. Therefore, it is likely there is another phenomenon causing the distinct curve of the plot, which isn't caused by dissolution, surface exchange kinetics, or dissolution, conforming that this complex mass transport cannot and should not be predicted by these models alone.

4.3.3 Statistical analysis. To assess the model's predictive accuracy, residuals analysis was conducted. Residual plots, generated according to eqn (12), were examined for random distribution around the horizontal zero line, a characteristic of well-fitting models. Positive residuals indicate under-prediction by the model whereas negative residuals indicate over-prediction. The single source and combined source model residual plots are shown in Fig. 19 and 22, respectively.

$$\text{Residuals} = \text{observed value} - \text{predicited value} \quad (12)$$

For the single-source mechanisms, all residual plots exhibited non-random patterns, deviating from scatter around the zero line (Fig. 22). For the 1% Sr loaded samples, a consistent trend was observed across all models: under-prediction at early time points, over-prediction in the mid-range, and under-prediction at later time points. The models exhibited slight variation in the final stages, with DIF under-predicting, DIS over-predicting, and SEK providing an accurate estimation. This discrepancy arises from the inverted, 'S' shape of the curve, which the models are unable to fully capture. A similar trend was observed for the 3% Sr loaded samples, although the DIF model over-predicted at the latter time points. Despite the non-random residuals, the magnitude of the residuals is consistently low, indicating little deviation between the observe values and the model predictions.

The residual plots for the Cs-containing samples showed distinct patterns between the models. The DIF and DIS models exhibited under- and over-prediction trends, expected due to their poor overall fits. However, the SEK model exhibits relatively well-distributed residuals, with a slight over- and under-prediction pattern. These are small in magnitude, indicating a reasonable fit. The residuals plots for the combined source models exhibit similar patterns for both Cs and Sr samples (Fig. 23). These consistent trends suggest that the models are not fully capturing the complex release behaviour, and therefore there may be additional mass transport contributing to the release.

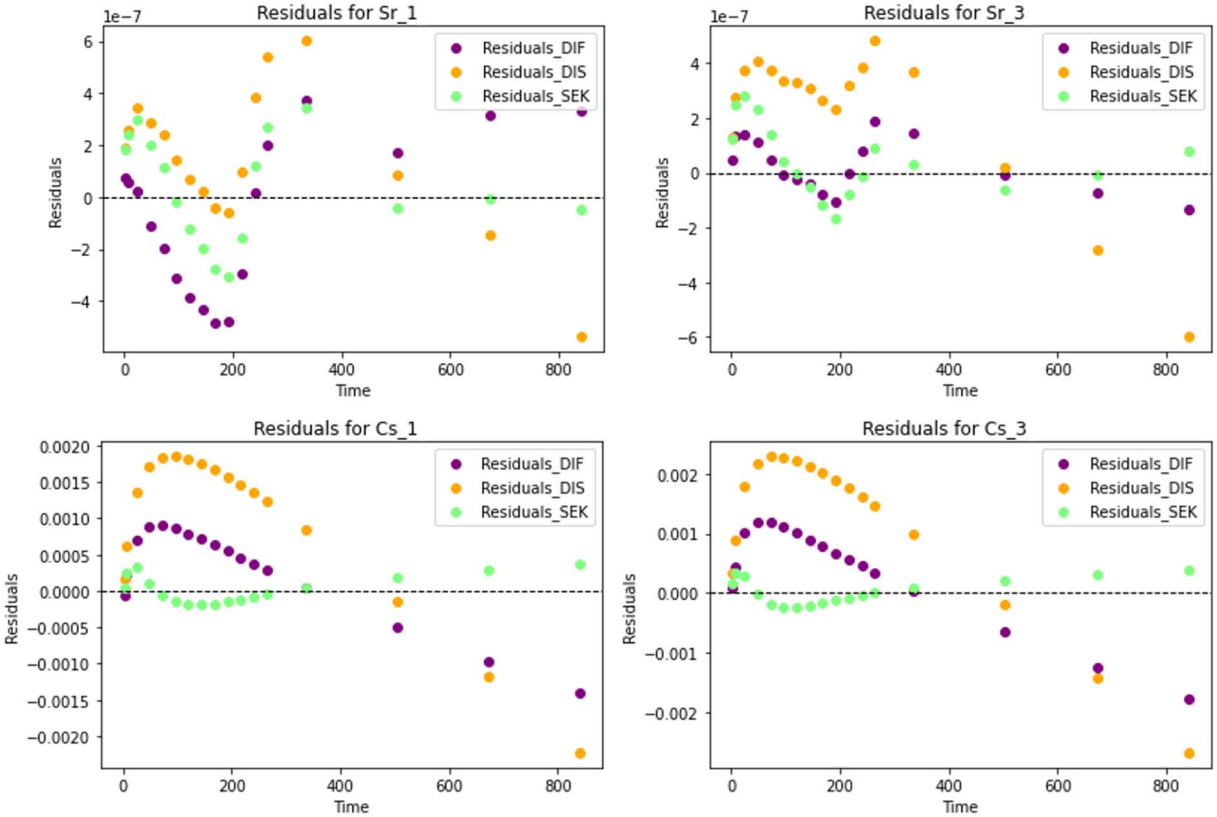

Fig. 22 Residuals plots for each single source model.

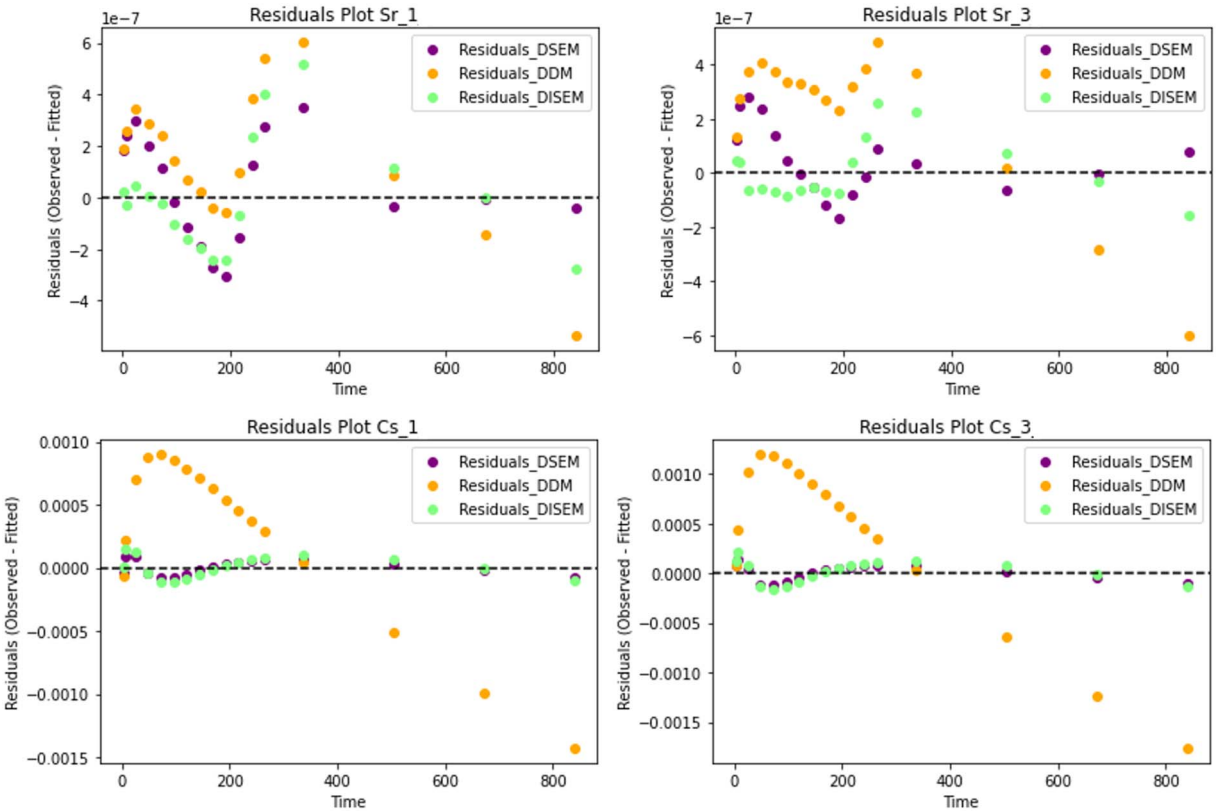

Fig. 23 Residuals plots for each combined source model.

5 Conclusions

This study investigated the performance and leaching mechanisms of Cs- and Sr-loaded geopolymers. Leaching tests revealed that Cs exhibits higher leachability than Sr, with distinct, different release patterns: Sr displays a staggered release, while Cs showed a smooth, consistent release. However, all samples out-performed PC/BFS blends under comparable conditions and significantly exceeded the industry minimum accepted value.

Structural analysis across XRD, SEM-EDX, EPMA, FTIR, and NMR revealed minimal impact of Cs and Sr incorporation or leaching on the geopolymer bulk structure. While element-specific NMR and XAS showed subtle changes in the immediate environment of the Cs and Sr after leaching, these did not significantly impact the bulk structure over the 35-day timeframe of the leach test and release rates were lower than for Portland cement wasteforms.

Finally, mass transport modelling did not produce a satisfactory fit to Sr data due to processes occurring not accounted for in the models. It is hypothesised that K–A–S–H gel reordering to form crystalline zeolite may account for the sudden increase in Sr release rates observed in the data. This presents implications for modelling the long-term performance of Sr in geopolymers destined for disposal as its long-term performance cannot be modelled using these processes. Nevertheless, even accounting for this rate resumption, Sr release rates remain very low. Further work will aim to understand the behaviour over longer timescales. In contrast, Cs release could be fit with a mixed model combining surface exchange kinetics and diffusion, with negligible contribution from dissolution.

To conclude, the geopolymer wasteforms, when leached in deionised water at 20 °C, are considered safe within the parameters of this study. Future work will explore more realistic disposal scenarios, such as increased temperature, radiation damage, and the use of clinoptilolite (ion exchange material) in disposal. Longer term experiment could explore the hypothesised mechanisms responsible for Sr's staggered release and whether this behaviour persists over longer time frames.

Conflicts of interest

There are no conflicts to declare.

Data availability

All data supporting this article have been included as part of the main manuscript.

Supplementary information (SI) is available. See DOI: https://doi.org/10.1039/d5ta08377j.

Acknowledgements

This work has been funded by the Engineering and Physical Sciences Research Council (EPSRC), UK, through EPSRC PhD studentship 2602279, part of the EPSRC CDT GREEN (EP/S022295/1), with co-funding from Sellafield Ltd., and grant EP/Y029208/1. The UK High-Field Solid-State NMR Facility used in this work was funded by EPSRC and BBSRC (grant EP/T015063/1), as well as the University of Warwick, including *via* part funding through Birmingham Science City Advanced Materials Projects 1 and 2 supported by Advantage West Midlands (AWM), and the European Regional Development Fund (ERDF). We acknowledge Diamond Light Source for time on Beamline B18 under Proposal SP37458-1, and thank Dr Thokozile Kathyola, Beamline Scientist, B18, Diamond Light Source, for assistance with acquiring the XAS data. We thank and acknowledge Dr Khalid Doudin, School of Maths, Physics, and Chemistry, The University of Sheffield, for assistance in acquiring some of NMR data obtained at The University of Sheffield, Dr Sarah Pepper, Royce Discovery Centre, The University of Sheffield, for assistance in acquiring some of the ICP data, and Dr Stuart Creasey-Gray, Sorby Centre for Electron Microscopy, The University of Sheffield, for assistance in acquiring some of the EPMA data.

References

1 B. Walkley, X. Ke, O. H. Hussein, S. A. Bernal and J. L. Provis, Incorporation of strontium and calcium in geopolymer gels, *J. Hazard. Mater.*, 2020, **382**, 121015, DOI: 10.1016/j.jhazmat.2019.121015.

2 A. M. James, S. Harding, T. Robshaw, N. Bramall, M. D. Ogden and R. Dawson, Selective environmental remediation of strontium and cesium using sulfonated hyper-cross-linked polymers (shcps), *ACS Appl. Mater. Interfaces*, 2019, **11**(25), 464–473, DOI: 10.1021/acsami.9b06295.

3 E. Duque-Redondo, K. Yamada and H. Manzano, Cs retention and diffusion in c-s-h at different ca/si ratio, *Cem. Concr. Res.*, 2021, **140**, 106–294, DOI: 10.1016/j.cemconres.2020.106294.

4 S. Bagosi and L. J. Csetényi, Caesium immobilisation in hydrated calcium-silicate-aluminate systems, *Cem. Concr. Res.*, 1998, **28**(12), 1753–1759, DOI: 10.1016/S0008-8846(98)00163-X.

5 S. Kearney, A. S. Yorkshire, D. A. Geddes, *et al.*, "Chapter 25 – cement-based stabilization/solidification of radioactive waste", in *Low Carbon Stabilization and Solidification of Hazardous Wastes*, ed. D. C. W. Tsang and L. Wang, Elsevier, 2022, pp. 407–431, DOI: 10.1016/B978-0-12-824004-5.00005-0.

6 J. Provis and J. Van Deventer, *Alkali Activated Materials: State-Of-The-Art Report, RILEM TC 224-AAM*, Springer, 2014, DOI: 10.1007/978-94-007-7672-2.

7 Q. Tian, S. Nakama and K. Sasaki, Immobilization of cesium in fly ash-silica fume based geopolymers with different si/al molar ratios, *Sci. Total Environ.*, 2019, **687**, 1127–1137, DOI: 10.1016/j.scitotenv.2019.06.095.

8 A. N. Society, *"Ansi/ans-16.1-2003: Measurement of the Leachability of Solidified Low-Level Radioactive Wastes by a Short-Term Test Procedure"*, American Nuclear Society, Tech. Rep., 2003, 2003.

9 P. L. Côté, T. W. Constable and A. Moreira, An evaluation of cement-based waste forms using the results of approximately two years of dynamic leaching, *Nucl. Chem. Waste Manage.*, 1987, **7**(2), 129–139, DOI: 10.1016/0191-815X(87)90007-6.
10 R. O. Abdel Rahman and A. A. Zaki, Comparative study of leaching conceptual models: Cs leaching from different ilw cement based matrices, *Chem. Eng. J.*, 2011, **173**(3), 722–736, DOI: 10.1016/j.cej.2011.08.038.
11 A. Abdel Rahman and R. O. Zaki, Assessment of the leaching characteristics of incineration ashes in cement matrix, *Chem. Eng. J.*, 2009, **155**, 698–708, DOI: 10.1016/j.cej.2009.09.002.
12 A. M. El-Kamash, A. M. El-Dakroury and H. F. Aly, Leaching kinetics of 137cs and 60co radionuclides fixed in cement and cement-based materials, *Cem. Concr. Res.*, 2002, **32**(11), 1797–1803, DOI: 10.1016/S0008-8846(02)00868-2.
13 A. M. El-Kamash, M. R. El-Naggar and M. I. El-Dessouky, Immobilization of cesium and strontium radionuclides in zeolite-cement blends, *J. Hazard. Mater.*, 2006, **136**(2), 310–316, DOI: 10.1016/j.jhazmat.2005.12.020.
14 K. T. O'Donoghue, D. A. Geddes, M. Hayes and B. Walkley, Reaction mechanisms and kinetics in geopolymers incorporating strontium salts, *Dalton Trans.*, 2025, **54**(29), 337–348, DOI: 10.1039/D5DT01087J.
15 R. Snellings, J. Chwast, Ö. Cizer, *et al.*, Rilem tc-238 scm recommendation on hydration stoppage by solvent exchange for the study of hydrate assemblages, *Mater. Struct.*, 2018, **51**(6), 172, DOI: 10.1617/s11527-018-1298-5.
16 E. Hespe, Leach testing of immobilized radioactive waste solids a proposal for a standard method, *Atom. Energy Rev.*, 1971, **9**(1), 195–207.
17 E. Mukiza, Q. T. Phung, L. Frederickx, D. Jacques, S. Seetharam and G. De Schutter, Co-immobilization of cesium and strontium containing waste by metakaolin-based geopolymer: Microstructure, mineralogy and mechanical properties, *J. Nucl. Mater.*, 2023, **585**, 154–639, DOI: 10.1016/j.jnucmat.2023.154639.
18 M. Arbel-Haddad, Y. Harnik, Y. Schlosser and A. Goldbourt, Cesium immobilization in metakaolin-based geopolymers elucidated by 133cs solid state nmr spectroscopy, *J. Nucl. Mater.*, 2022, **562**, 153–570, DOI: 10.1016/j.jnucmat.2022.153570.
19 M. Arbel Haddad, E. Ofer-Rozovsky, G. Bar-Nes, *et al.*, Formation of zeolites in metakaolin-based geopolymers and their potential application for cs immobilization, *J. Nucl. Mater.*, 2017, **493**, 168–179, DOI: 10.1016/j.jnucmat.2017.05.046.
20 T. Skorina, Ion exchange in amorphous alkali-activated aluminosilicates: Potassium based geopolymers, *Appl. Clay Sci.*, 2014, **87**, 205–211, DOI: 10.1016/j.clay.2013.11.003.
21 R. G. Newton, Durability of glass - a review, *Glass Technol.*, 1985, **26**(1), 21–38.
22 F. Frizon, S. Gin and C. Jegou, "Mass transfer phenomena in nuclear waste packages", in *Advances in Transport Phenomena: 2009*, ed. L. Wang, Springer Berlin Heidelberg, Berlin, Heidelberg, 2009, pp. 31–133, DOI: 10.1007/978-3-642-02690-4_2.
23 P. Frugier, S. Gin, Y. Minet, *et al.*, Son68 nuclear glass dissolution kinetics: Current state of knowledge and basis of the new graal model, *J. Nucl. Mater.*, 2008, **380**(1), 8–21, DOI: 10.1016/j.jnucmat.2008.06.044.
24 A. Ait Chaou, A. Abdelouas, Y. El Mendili and C. Martin, The role of ph in the vapor hydration at 175 °c of the french son68 glass, *Appl. Geochem.*, 2017, **76**, 22–35, DOI: 10.1016/j.apgeochem.2016.11.006.
25 J.-Y. Goo, B.-J. Kim, M. Kang, J. Jeong, H. Y. Jo and J.-S. Kwon, Leaching behavior of cesium, strontium, cobalt, and europium from immobilized cement matrix, *Appl. Sci.*, 2021, **11**(18), 8418.
26 V. A. Baki, Enhancing the reactivity of natural minerals as supplementary cementitious materials for low-carbon binders, PhD thesis, University of Bath, 2023.
27 K. Lee and J. Kim, Immobilization of 137cs as a crystalline pollucite surrounded by amorphous aluminosilicate, *Environ. Res.*, 2023, **221**, 115–309, DOI: 10.1016/j.envres.2023.115309.
28 A. Hajimohammadi, J. L. Provis and J. S. J. van Deventer, The effect of silica availability on the mechanism of geopolymerisation, *Cem. Concr. Res.*, 2011, **41**(3), 210–216, DOI: 10.1016/j.cemconres.2011.02.001.
29 W. K. W. Lee and J. S. J. van Deventer, Use of infrared spectroscopy to study geopolymerization of heterogeneous amorphous aluminosilicates, *Langmuir*, 2003, **19**(21), 8726–8734, DOI: 10.1021/la026127e.
30 E. Ofer-Rozovsky, M. A. Haddad, G. Bar-Nes, *et al.*, Cesium immobilization in nitrate-bearing metakaolin-based geopolymers, *J. Nucl. Mater.*, 2019, **514**, 247–254, DOI: 10.1016/j.jnucmat.2018.11.003.
31 A. Mekki, A. Benmaati, A. Mokhtar, M. Hachemaoui, F. Zaoui, H. Habib Zahmani, B. Boukoussa, *et al.*, Michael addition of 1,3-dicarbonyl derivatives in the presence of zeolite y as an heterogeneous catalyst, *J. Inorg. Organomet. Polym. Mater.*, 2020, **30**(7), 2323–2334, DOI: 10.1007/s10904-019-01424-5.
32 B. Walkley and J. L. Provis, Solid-state nuclear magnetic resonance spectroscopy of cements, *Mater. Today Adv.*, 2019, **1**, 100007, DOI: 10.1016/j.mtadv.2019.100007.
33 D. A. Geddes, M. C. Stennett, T. J. Wilkinson, B. E. Griffith, J. V. Hanna, J. L. Provis, B. Walkley, *et al.*, Alkali-mediated sr incorporation mechanism and binding capacity of alkali aluminosilicate hydrate in geopolymers, *J. Hazard. Mater.*, 2025, **488**, 137426, DOI: 10.1016/j.jhazmat.2025.137426.
34 F. Yagi, N. Kanuka, H. Tsuji, S. Nakata, H. Kita and H. Hattori, 133cs and 23na mas nmr studies of zeolite x containing cesium, *Microporous Mater.*, 1997, **9**(5), 229–235, DOI: 10.1016/S0927-6513(96)00113-7.
35 A. Materials, Type a and x zeolites, Web Page, n.d.
36 A. Medek, J. S. Harwood and L. Frydman, Multiple-quantum magic-angle spinning nmr: A new method for the study of quadrupolar nuclei in solids, *J. Am. Chem. Soc.*, 1995, **117**(51), 779–787, DOI: 10.1021/ja00156a015.

